ELSEVIER

Contents lists available at ScienceDirect

### Computers and Geotechnics

journal homepage: www.elsevier.com/locate/compgeo



# Nanoscale soil-water retention mechanism of unsaturated clay via MD and machine learning

Zhe Zhang, Xiaoyu Song \*

Department of Civil and Coastal Engineering, University of Florida, Florida, Gainesville, United States

#### ARTICLE INFO

Keywords: Soil-water retention Interfacial area Unsaturated clay Adsorption Machine learning

#### ABSTRACT

In this article, we investigate the nanoscale soil-water retention mechanism of unsaturated clay through molecular dynamics and machine learning. Pyrophyllite was chosen due to its stable structure and as the precursor of other 2:1 clay minerals. A series of molecular dynamics simulations of clay at low degrees of saturation were conducted. Soil water was represented by a point cloud through the center-of-mass method. Water-air interface area was measured numerically by the alpha-shape method. The soil-water retention mechanism at the nanoscale was analyzed by distinguishing adsorptive pressure and capillary pressure at different mass water contents and considering the apparent capillary interface area (i.e., water-air interface area per unit water volume). The water number density profile was used to quantify the adsorption effect. A neural-network based machine learning technique was utilized to construct functional relationships among matric suction, the mass water content, and the apparent water-air interface area. Our numerical results have demonstrated from a nanoscale perspective that the adsorption effect is dominated by the van der Waals force and hydroxyl hydration between the clay surface and water. As the mass water content increases, the adsorption pressure decreases, and capillarity plays a prominent role in the soil-water retention mechanism at the nanoscale.

#### 1. Introduction

The physics and mechanics of unsaturated soils are important in geotechnical and geoenvironmental engineering (e.g., Terzaghi et al., 1996; Gens, 2010; Fredlund, 2006; Ng and Menzies, 2014; Song, 2017; Alonso, 2021; Menon and Song, 2022, 2023). Soil-water retention/ characteristic curve (SWRC) is a mathematical relationship between soil water content and matric suction (e.g., Brooks, 1965; Van Genuchten, 1980; Fredlund and Rahardjo, 1993; Fredlund and Xing, 1994; Niu et al., 2020; Cao et al., 2018; Chen et al., 2019). It is a fundamental constitutive law for modeling the physics and mechanics of unsaturated soils. For instance, a soil water retention curve is required in modeling multiphase fluid flow, shear strength, deformation, and stress-strain relationships of unsaturated soils (e.g., Alonso et al., 1990; Wheeler et al., 2003; Macari et al., 2003; Hoyos and Arduino, 2008; Alonso et al., 2010). In unsaturated soil mechanics and continuum-based numerical methods for modeling unsaturated soils with no osmosis effect, matric suction is usually assumed to be the difference between pore air pressure and pore water pressure and the latter is usually assumed to be the capillary pressure due to water meniscus (e.g., Fredlund and Rahardjo,

1993; Borja, 2004, 2006; Menon and Song, 2020, 2021; Song et al., 2017; Wang and Song, 2020) without considering adsorptive water pressure. The adsorptive water pressure might be ignored at a high degree of saturation. However, at a low degree of saturation, it should be considered to interpret high matric suction (e.g., on the order of hundred megapascals) (Fredlund and Rahardjo, 1993; Lu and Likos, 2006; Zhang and Lu, 2019). It is noted that the pressure of capillary water is lower than air pressure due to the curve water-air interface (i.e., meniscus), and pressure of adsorptive water is higher than air pressure due to adsorptive force (Luo et al., 2022). Furthermore, both experimental and theoretical studies have suggested that the water-air interface should be taken into account to better describe soil water retention curves of unsaturated soils (Fredlund and Morgenstern, 1977; Hassanizadeh and Gray, 1990; Joekar-Niasar et al., 2008; Lourenc o et al., 2012; Lu and Likos, 2006; Likos, 2014; Fredlund, 2006). We refer to the related literature for a thermodynamic justification (e.g., Houlsby, 1997; Nikooee et al., 2013) of including the water-air interface in the soilwater retention curve of unsaturated soils. In Fredlund and Morgenstern (1977), the water–air interface was first incorporated into stress analysis of unsaturated soils where the air-water interface is treated as an

E-mail address: xysong@ufl.edu (X. Song).

 $<sup>^{\</sup>ast}$  Corresponding author.

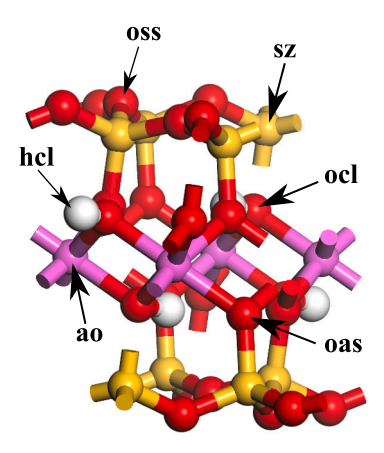


Fig. 1. Unit cell of pyrophyllite.

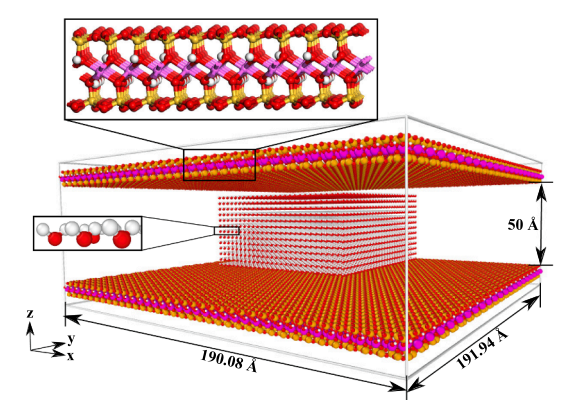


Fig. 2. Initial configuration of the clay-water model.

independent phase. In Lu and Likos (2006), the interfacial effects are lumped into the suction stress in addition to capillary pressure. In Nikooee et al. (2013), the interfacial energy and air—water specific interfacial area are integrated into an effective stress tensor using a thermodynamic approach. Interfacial force arises due to the unbalanced force exerted on two sides of interfaces, which may influence the macroscopic soil behavior. Several physicochemical effects contribute to the origin of interface force, such as van der Waals forces, surface tension, and electric double-layer forces. These interface forces could produce surface energy change and deformation of soil (Butt et al., 2013).

Over the past decades, computational modeling through physicsbased numerical methods has gained success in resolving and quantifying water-air interfaces in porous media. One standard method is the pore-network modeling technology (Lowry and Miller, 1995; Joekar-Niasar et al., 2008). Several techniques have also been developed to measure the water-air interface area in porous media (Costanza-Robinson and Brusseau, 2002; Chen and Kibbey, 2006; Wildenschild et al., 2002; Brusseau et al., 2007; Lourenc o et al., 2012). However, the configuration of pore network is user-defined instead of the actual pore space in nature. Moreover, it remains challenging to quantify the impact of adsorption on SWRC and explain the mechanism of soil-water adsorption at the nanoscale. At the nanoscale adsorptive forces in finegrained clay become pronounced and could modify the water structure, e.g., adsorptive water film tightly attached to clay surface (Evans et al., 1986; Tuller et al., 1999). It is noted that the laboratory measurement techniques only suffice to account for capillary effects in the water retention mechanism (Likos et al., 2019). Indeed no viable experimental technique exists to quantify adsorption and its impact on SWRC in unsaturated soils at the nanoscale (Lu, 2016).

As a numerical method at the atomic scale, molecular dynamics

(MD) can naturally consider adsorption at the nanoscale. With advances in high-performance supercomputers, MD simulations have been extensively used to gain detailed insights into the physics and mechanics of unsaturated soils at the atomic scale (e.g., Cygan et al., 2004; Katti et al., 2015; Song and Zhang, 2021; Song et al., 2018; Song and Wang, 2019). MD is a computational simulation technique that numerically solves Newton's equations of a classical N-body system at equilibrium (Frenkel and Smit, 2001; Allen and Tildesley, 2017; Plimpton, 1995). It is a viable numerical tool to study the effect of soil-water interactions on the physics and mechanics of unsaturated soils. The strong atomic interaction across the clay-water interface could cause a divergence from the bulk phase behavior of water. Examples include capillary condensation and solid-water adsorption (e.g., Shi and Dhir, 2009; Leroy and Muller-Plathe, 2010; Scocchi et al., 2011; Botan et al., 2011). To the best of our knowledge, few studies have used MD simulations to investigate soil-water retention curves accounting for water-air interface and soil-water adsorption. In this article, MD is utilized to study the impacts of the water-air interface and soil-water adsorption on the nanoscale soil-water retention mechanism at low degrees of saturation.

The area of the water-air interface (i.e., concave water meniscus) in unsaturated soils is nontrivial to compute from the MD simulation data. In this article, the point cloud method coupled with surface reconstruction, as detailed in Section 2, will be used to calculate the water-air interface area at different degrees of saturation (water mass content). Note that surface reconstruction is a subject in computer graphics that deals with surface/shape properties of a point set, such as surface normal estimation (Boissonnat, 1984; Edelsbrunner and Mucke, 1994). Among various surface reconstruction techniques, the alpha-shape method has been successfully employed to characterize the shape of molecules like proteins (Peters et al., 1996; Liang et al., 1998). In Wilson et al. (2009), the author validated the robustness and effectiveness of the alpha-shape method in characterizing the shapes of small molecules compared to other shape predictors. In Singh et al. (1996), the authors applied the alpha-shape method in molecular recognition and identified binding sites in proteins. Inspired by the broad applications in molecular biology, in this study, the alpha-shape method was utilized to calculate the water-air interface area from the MD results. Section 2 presents the unsaturated clay model for the MD simulations and the alpha shape method for the interfacial area calculation. Section 3 concerns the numerical results of the water-air interface area, capillary and adsorptive pressures and conducts data analytics regarding SWRC through a machine-learning curve fitting technique. Section 4 compares the nanoscale water retention mechanisms of kaolinite and pyrophyllite and discusses the effect of clay particle configurations and pore sizes on the clay-water retention mechanism, followed by a summary in Section 5.

#### 2. Material model and MD modeling

In this study, pyrophyllite that is a 2:1 clay mineral composed of silicon tetrahedral and aluminum octahedral layers was chosen due to its stable structure and being a precursor to other smectite clay minerals. The aluminum octahedral (O) sheet is bounded by two opposing silicon tetrahedral (T) sheets, which form a T-O-T structure. The chemical formula of pyrophyllite is  $Al_2[Si_4O_{10}](OH)_2$ . The unit cell of pyrophyllite has the dimensions of 5.28 Å  $\times$  9.14 Å  $\times$  6.56 Å in the x-y-z Cartesian coordinate system (Skipper et al., 1995).

Fig. 1 shows one unit cell of pyrophyllite made up of six types of atoms. In Fig. 1, ao is aluminum in the octahedral layer, ocl and hcl are oxygen and hydrogen in the octahedral layer that form the covalent hydroxyl bond, sz is silicon in the tetrahedral layer, oss is oxygen in Si-O-Si linkages, and oas is oxygen in Si-O-Al linkages in the tetrahedral layer. Unlike other smectite clay minerals with a strong cation exchange capacity, pyrophyllite has a weak capacity to swell or shrink because of its neutral surface charge. Considering its structural stability, the clay particle is treated as a rigid body, and its motion was frozen during the simulation.

**Table 1**Values of the input parameters for CHARMM force field.

Symbol	$q_i(e)$	$\epsilon_i(\text{kcal/mol})$	$R_i(\mathring{A})$
hw	0.417	0.046	0.44
ow	-0.834	0.152	3.53
ocl	-0.96	6	2.8
hcl	0.4	0.0001	2.4
oas	-0.91	6	2.8
oss	-0.7	1	3
SZ	1.4	0.001	7.4
ao	1.68	0.15	6.3

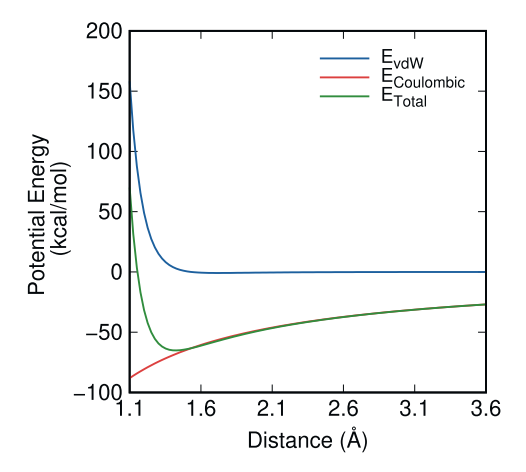


Fig. 3. Interactions between clay surface oxygen (oss) and water hydrogen (hw) as a function of the interatomic distance.

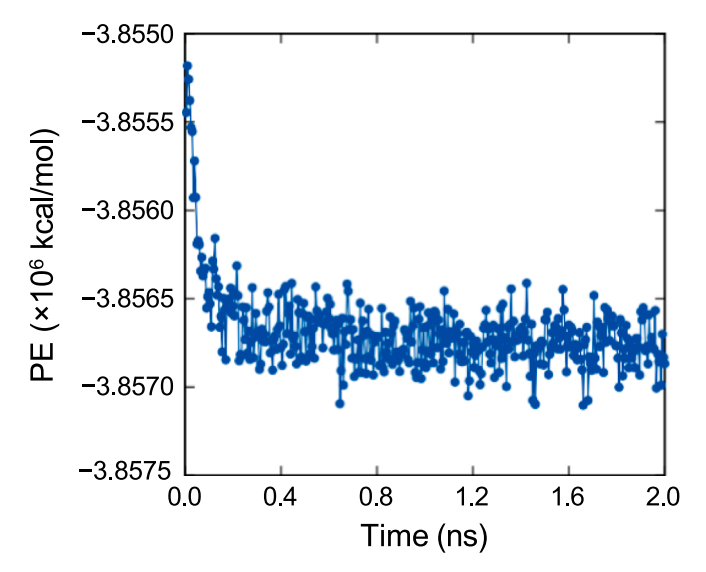


Fig. 4. Variation of potential energy during the MD simulation.

Fig. 2 shows the initial configuration of the clay-water model. Each clay layer consists of  $36 \times 21 \times 1$  unit cells in the x-y-z directions, corresponding to 190.08 Å  $\times$  191.94 Å in the x-y plane. Water is modeled by the TIP3P model (Jorgensen et al., 1983). Water molecule was considered a rigid body during the simulation. The space between the parallel clay layers is d=50 Å which could avoid any possible interlayer interactions between clay plates (Amarasinghe et al., 2014).

In this study, CHARMM force field (Brooks et al., 1983) is employed to describe the soil–water interaction in that CHARMM force field is compatible with the TIP3P water model (Berendsen et al., 1987). CHARMM force field has been widely utilized to study clay-water

systems (Katti et al., 2015; Song and Wang, 2019). The non-bonded potential energy U in the CHARMM force field can be defined as

$$U = \sum_{i \neq j} 4 \epsilon_{ij} \left[ \left( \frac{R_{ij}}{r_{ij}} \right)^{12} - \left( \frac{R_{ij}}{r_{ij}} \right)^{6} \right] + \sum_{i \neq j} \frac{q_{i}q_{j}}{4\pi\epsilon_{0}r_{ij}}, \tag{1}$$

where  $\varepsilon_{ij}$  is the well-depth of Lennard-Jones (LJ) potential and  $R_{ij}$  is the distance at the minimum LJ interaction energy,  $q_i$  and  $q_j$  are the charge of atoms i and j, respectively,  $\varepsilon_0$  is the vacuum permittivity,  $r_{ij}$  is the distance between atoms i and j. In this study, clay particles are assumed immobilized and only non-bonded interactions between clay and water were simulated (Song et al., 2018).

The cutoff radii for van der Waals and Coulombic interactions are 10 Å. Table 1 lists the nonbonded parameters for the clay-water system. Note that hw and ow denote water hydrogen and water oxygen, respectively. Fig. 3 presents an example of nonbonded interactions (i.e., van der Waals energy and Coulombic energy) between clay surface oxygen (oss) and water hydrogen (hw) as a function of interatomic distance. The interaction between oss and hw was chosen as an example because of the strong clay-water interaction such as surface hydration between the two types of atoms. The minimum potential energy occurs when the two atoms are at a distance of 1.4 Å. This indicates that the forces between the two atoms are repulsive within the distance of 1.4 Å.

All MD simulations were performed on LAMMPS, a large-scale atomic/molecular massively parallel simulator (Plimpton, 1995) using NVT ensemble at 298 K. Periodic boundary conditions were assigned in all directions. Water molecules were kept rigid using the SHAKE algorithm (Ryckaert et al., 1977) with constraints applied to hydrogen bonds and angles. The velocity Verlet algorithm with a time step of 0.5 fs (1 fs =  $1 \times 10^{-15}$  s) was employed to integrate the equations of motion of water. The simulation was first run for 2 ns to bring the system into equilibrium. Then the production simulation was run for 1 ns to output averaged water trajectories and water pressure. The potential energy profile was monitored to check the equilibrium state. Fig. 4 shows the time evolution of potential energy for the clay-water system during the equilibration. It can be seen that the system reached a dynamic equilibrium after 0.6 ns.

In this study, mass water content or moisture content ( $\Theta_g$ ) was chosen to represent the degree of water saturation. Mass water content is defined as the ratio between the mass of water and the mass of the solid

$$\Theta_g = \frac{N_w M_w}{N_v N_v N_w},\tag{2}$$

where  $N_w$  is the total number of water molecules,  $M_w \approx 18$  g/mol is the molar mass of water,  $M_p \approx 360$  g/mol is the molar mass of pyrophyllite, and  $N_x = 36$ ,  $N_y = 21$ , and  $N_z = 1$  are the number of unit cells in the x, y and z directions, respectively. The variation of mass water content was realized by adjusting the number of water molecules between the clay particles. The degree of saturation is calculated by

$$S_r = \Theta_g G_s / e, \tag{3}$$

where e is void ratio and  $G_s$  is specific gravity of dry clay. In MD, the pressure tensor of a group of atoms can be expressed through the virial stress tensor (Clausius, 1870) as

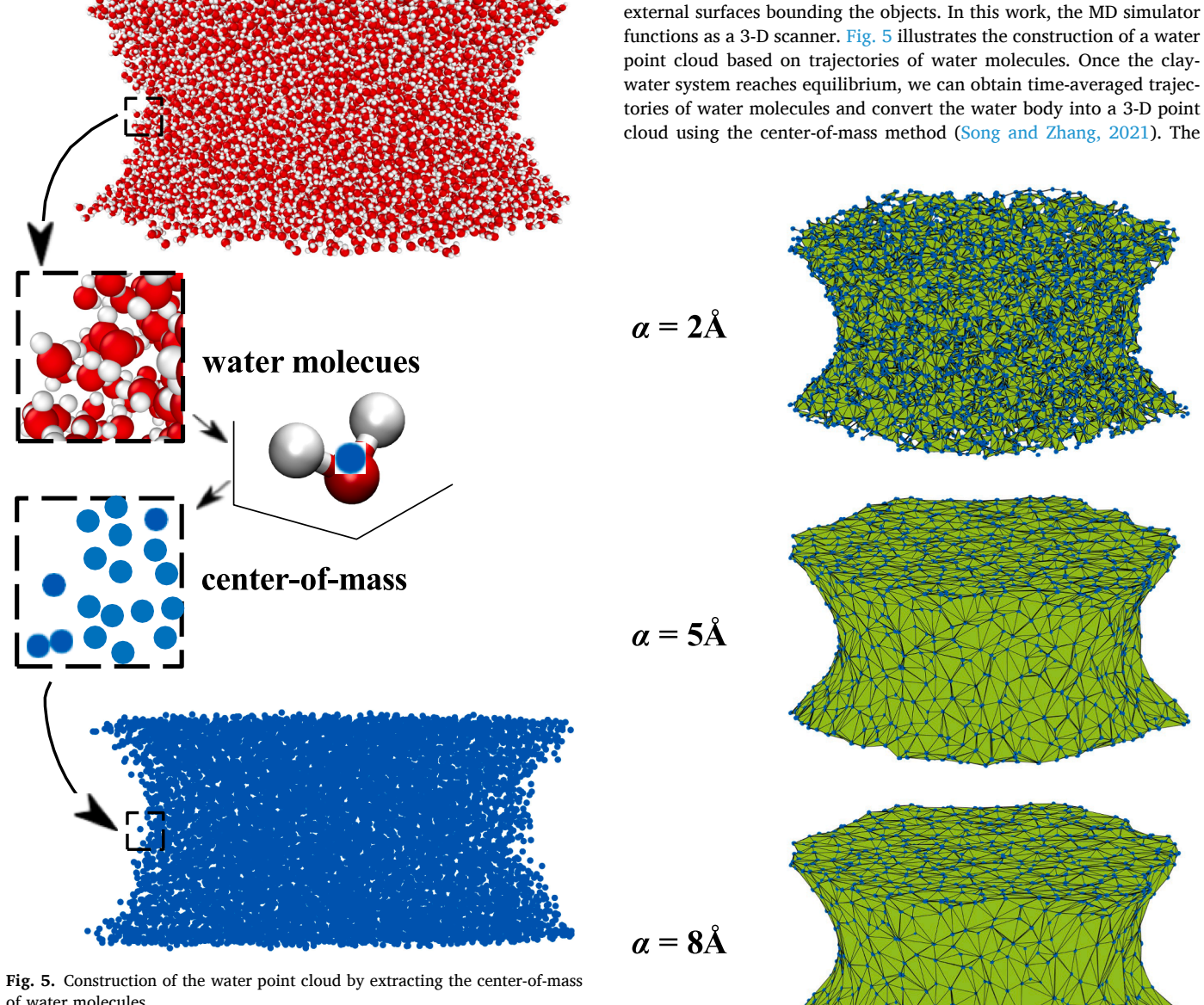
$$\sigma_{ij} = \frac{\sum_{k}^{N} m_k v_{ki} v_{kj}}{V} + \frac{\sum_{k}^{N} r_{ki} f_{kj}}{V},\tag{4}$$

where k is the atom index, N is the number of atoms in the water group, V is the volume of confined water, i, j = 1, 2, 3, and  $m_k, v_k, r_k$  and  $f_k$  denote the mass, velocity, position, and force of atom k, respectively. The pore water pressure can be determined from equation (4) as

$$p_{w} = \frac{1}{3}(\sigma_{11} + \sigma_{22} + \sigma_{33}), \tag{5}$$

Next, the method for determining the water–air interface area will be introduced.

adopted to determine the water-air interface area. Point clouds are commonly produced by 3D scanners, which collect points on the



of water molecules.

#### 2.1. Procedure of the interfacial area calculation via the alpha-shape method

In this study, the point cloud concept and alpha shape method were

**Fig. 7.** Comparison of alpha shapes of the water point cloud with  $\alpha=2$  Å, 5 Å, and 8 Å.

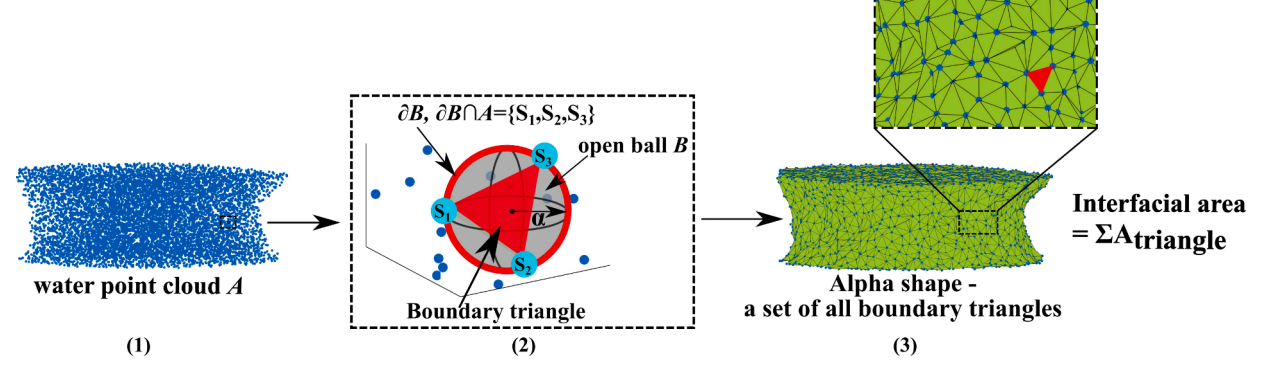


Fig. 6. Schematic procedure of the interfacial area calculation using the alpha-shape method.

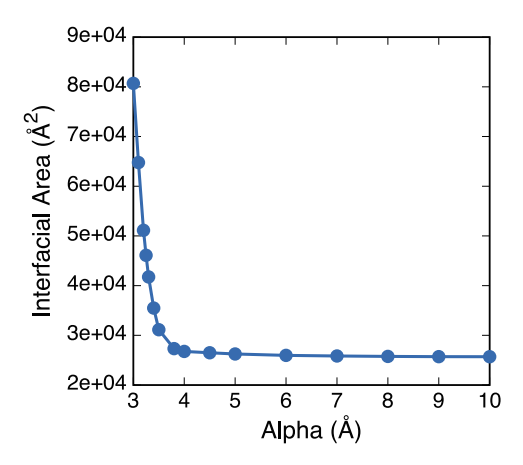


Fig. 8. Effect of the alpha value on total interfacial area.

**Table 2**Summary of the MD simulations in this study and their corresponding values of mass water content and degree of saturation.

Simulation No.	θ <sub>g</sub> (%)	S <sub>r</sub> (%)	Simulation No.	θ <sub>g</sub> (%)	$S_r(\%)$
1	6.2	2.3	2	7.3	2.8
3	8.4	3.2	4	9.7	4.0
5	11.0	4.7	6	12.4	5.4
7	13.9	6.1	8	14.7	6.3
9	15.5	6.9	10	17.2	7.6
11	18.1	8.0	12	19.0	8.5
13	20.8	9.5	14	22.7	10.5
15	24.8	10.6	16	26.9	12.0
17	27.9	12.6	18	29.1	13.6
19	31.3	14.7	20	32.5	15.1
21	33.7	16.0	22	34.9	16.2
23	36.2	17.3	24	37.4	17.4

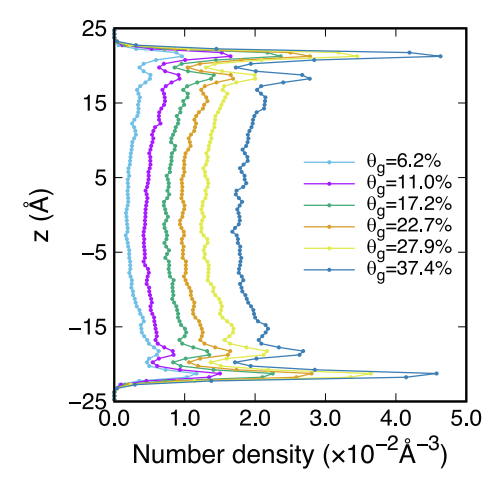


Fig. 9. Number density profiles of soil water at various mass water contents.

coordinate of center-of-mass  $r_{\rm c}$  of a water molecule can be expressed as

$$\mathbf{r}_c = \frac{\sum m_0 \mathbf{r}_0 + m_h(\mathbf{r}_{h1} + \mathbf{r}_{h2})}{m_0 + 2m_h},$$
 (6)

where m and r = (x, y, z) denote the atomic mass and Cartesian coordinate system vector, and subscripts o and h stands for water oxygen and hydrogen, respectively.

After obtaining the water point cloud, we reconstruct its surface using the alpha-shape method (Edelsbrunner and Mucke, 1994). The general idea is to find piece-wise triangles (the so-called alpha shapes) to represent the surface of the water point cloud. Fig. 6 shows the

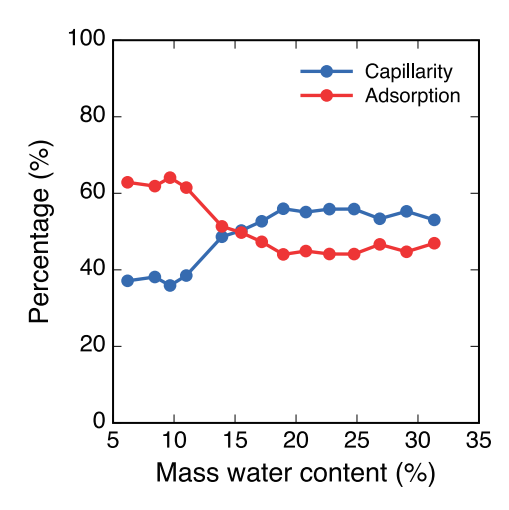


**Fig. 10.** Percentage of adsorptive and capillary water pressure as a function of mass water content.

**Table 3**Summary of percentages of adsorptive and capillary water pressures in the pore space for several MD simulations.

$\theta_{\rm g}(\%)$	Adsorption (%)	Capillarity (%)
6.2	62.9	37.1
7.3	58.1	41.94
8.4	61.9	38.1
9.7	64.1	35.9
11.0	61.5	38.5
13.9	51.4	48.6
15.5	49.7	50.3
17.2	47.3	52.7
20.8	44.9	55.1
24.	44.1	55.9
27.9	46.2	53.8
31.3	47.0	53.0
34.9	42.7	57.3
37.4	43.3	56.7

**Table 4**Sorptive energy between clay and adsorptive water at different mass water contents.

$\theta_g(\%)$	Sorptive energy (kcal/mol)
9.7	-263.9
11.0	-297.1
12.4	-328.3
13.9	-355.8
14.7	-371.3
17.2	-388.0
18.1	-424.2
20.8	-460.8
27.9	-597.5
31.3	-671.7
34.9	-721.5

schematic procedure of interfacial area calculation using the alphashape method. We could define a point set A where each point represents the center-of-mass of one water molecule. Let B be an open ball with radius  $\alpha$ . We restrict B to be empty such that it can occupy its space without enclosing any of the points of A, i.e.,  $B \cap A = \emptyset$ . Let  $T = \{S_i, S_j, S_k\}$  be a subset of A. Given T, we could define a 2-simplex  $\Delta_T$  (i.e., a triangle) as the convex hull of T. Here, the convex hull is the smallest convex set that contains all points in T (Barber et al., 1996). The 2-simplex is said to be  $\alpha$ -exposed if  $T = \partial B \cap A$ . Here,  $\partial B$  is the boundary of B.

For implementation, we first perform the Delaunay triangulation of the surface of the water point cloud and then define the alpha complex

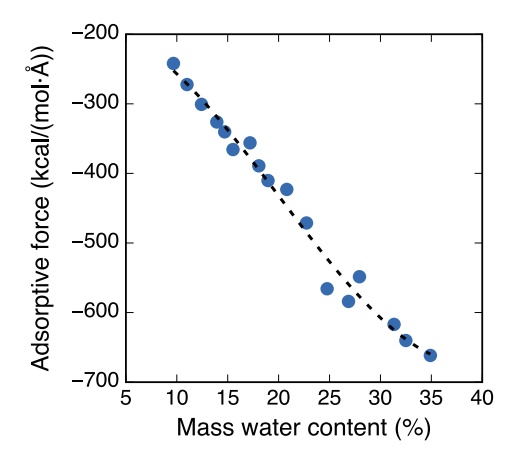


Fig. 11. Variation of the adsorptive force with mass water content.

that associates Delaunay triangulation with the alpha shape (Edelsbrunner and Mucke, 1994). The algorithm adopted is summarized as follows.

- (a) Compute the Delaunay triangulation of A, knowing that the boundary of  $\alpha$ -shape is contained in Delaunay triangulation.
- (b) Determine a-complex by inspecting all simplices DT in Delaunay triangulation. If the circumsphere of DT is empty and the radius of the circumsphere is smaller than  $\alpha$ , we accept DT as a member of  $\alpha$ -complex.
- (c) All simplices on the boundary of  $\alpha$ -complex form the  $\alpha$ -shape.

In Fig. 6 (2), the gray object is an empty open ball B, the red sphere is the boundary  $\partial B$ , and  $T = \partial B \cap A = \{S_i, S_j, S_k\}$ . Meanwhile, we must have  $B \cap A = \emptyset$  and B is exterior to A. The spherical cap is straightened by a 2-simplex (i.e., triangle in red) connected by points  $S_1, S_2$ , and  $S_3$ . Thus, the alpha shape of A is the polytope whose boundary consists of all the 2-simplices/triangles. The interfacial area is the sum of the area of each boundary triangle. The parameter  $\alpha$  controls the desired level of shape detail. We note that the critical  $\alpha$  calculated by MATLAB is assumed as the value of parameter  $\alpha$  in this study. It is the smallest alpha that produces an alpha shape with no inner cavities developed. Fig. 7

compares the configurations of alpha shapes when  $\alpha$  equals 2 Å, 5 Å, and 8 Å, respectively. Alpha smaller than the critical value produces cavities and would generate an unreasonable interfacial area. Fig. 8 shows the parameter  $\alpha$  sensitivity of the wetting-nonwetting interfacial area. The results correspond to a mass water content of 29.1%. The critical alpha for this case is 4.9 Å. It can be found that  $\alpha$  has little to no effect on the interfacial area when  $\alpha$  is greater than 5 Å. Thus, we assume  $\alpha=5$  Å in this study.

#### 3. Numerical results

In this section, we present the numerical results of capillary and adsorptive pressures, the water-air interface area and thickness at different mass water contents, and conduct data analytics regarding adsorptive and capillary water pressure curves through a machinelearning based curving fitting. Table 2 summarizes MD simulations with corresponding values of mass water content and degree of saturation. For each simulation, we computed pore-water pressure (capillary water pressure and adsorptive water pressure), water number density, and interface area and thickness. Through machine learning, we have generated the soil-water retention curve in terms of matric suction, mass water content, and apparent water-air interface area without prescribing a specific functional relationship among those variables. To demonstrate the usefulness of machine-learning based data analytics, the trained and validated neural network was used to predict the matric suction given a mass water content that is beyond the range of the MD simulations in this study.

#### 3.1. Adsorptive and capillary water pressures at the nanoscale

At the nanoscale, adsorption becomes important in the soil water retention mechanism. In general, the water in the nanoscale clay pore space can be assumed as discrete layers rather than a continuum as bulk water. Thus, in this study, the water number density profile from the MD results is utilized to distinguish adsorption and capillarity in pore water. First, the nanopore space is evenly divided into a number of parallel layers along the z direction. Then, the number density of each layer is computed as the number of water molecules divided by the volume of the layer. We note that water number density is computed for describing water distribution rather than mass density in that the local mass density

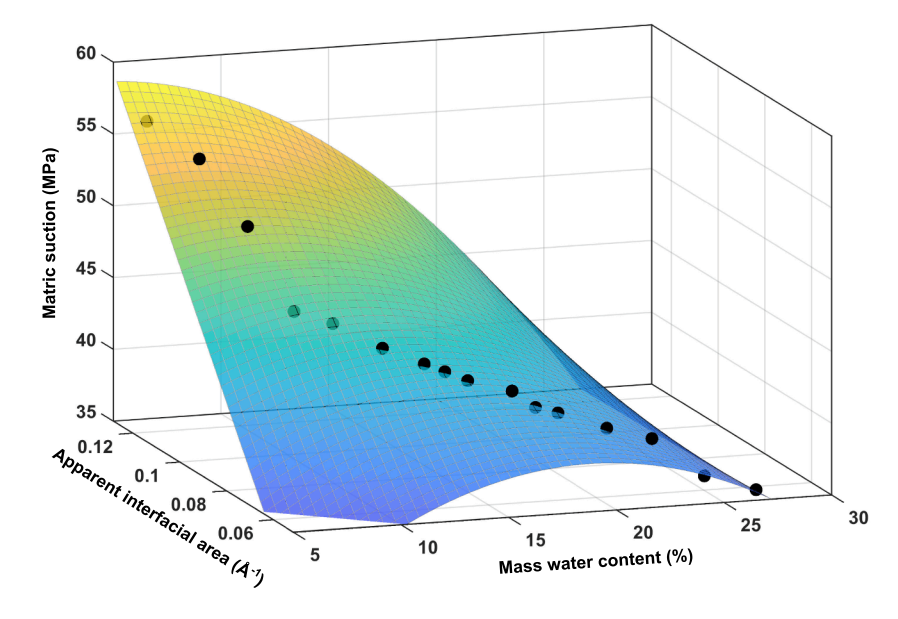


Fig. 12. Soil-water retention surface from the MD results through a standard curve fitting technique.

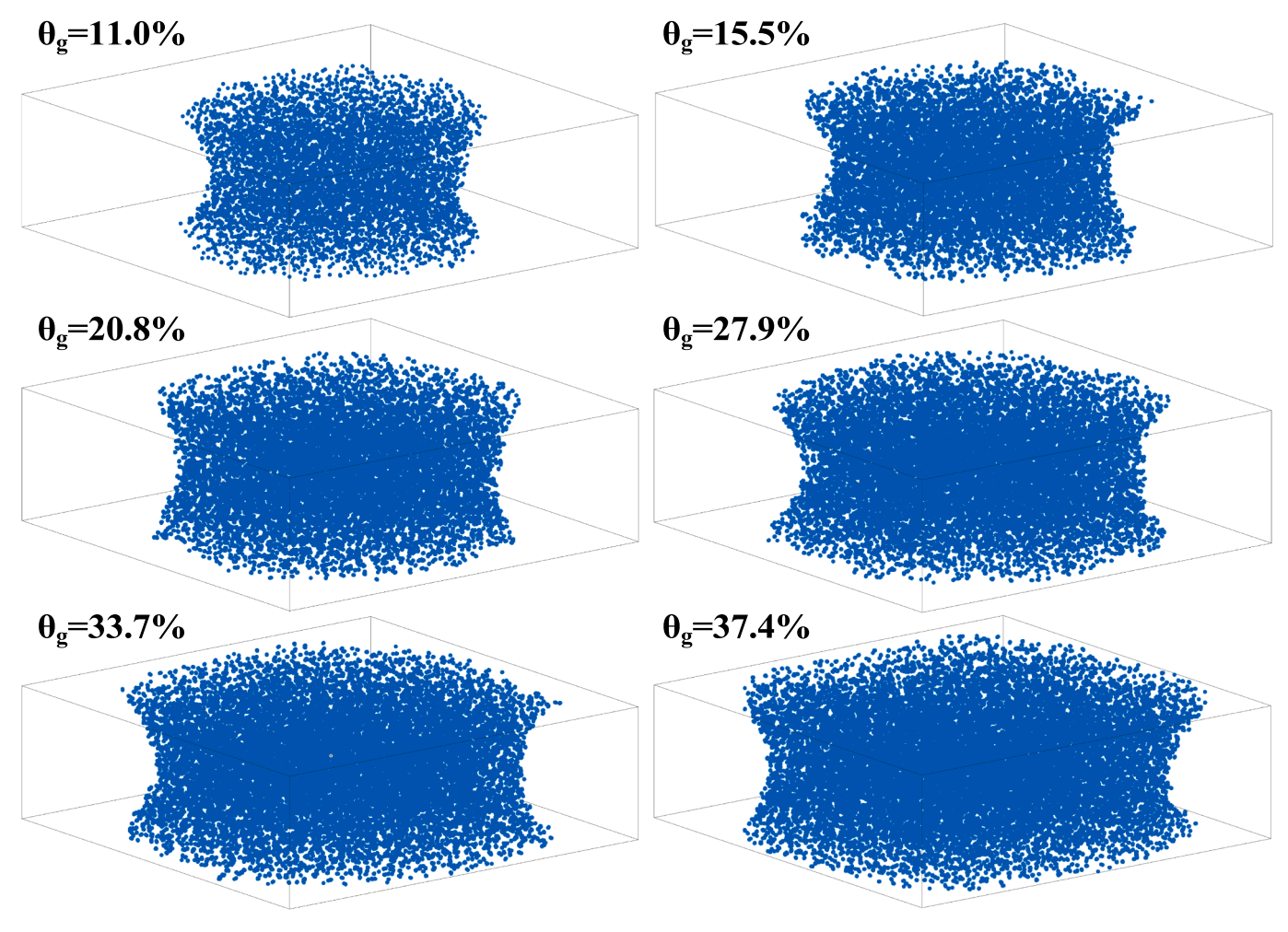


Fig. 13. Comparison of water point clouds for six mass water contents.

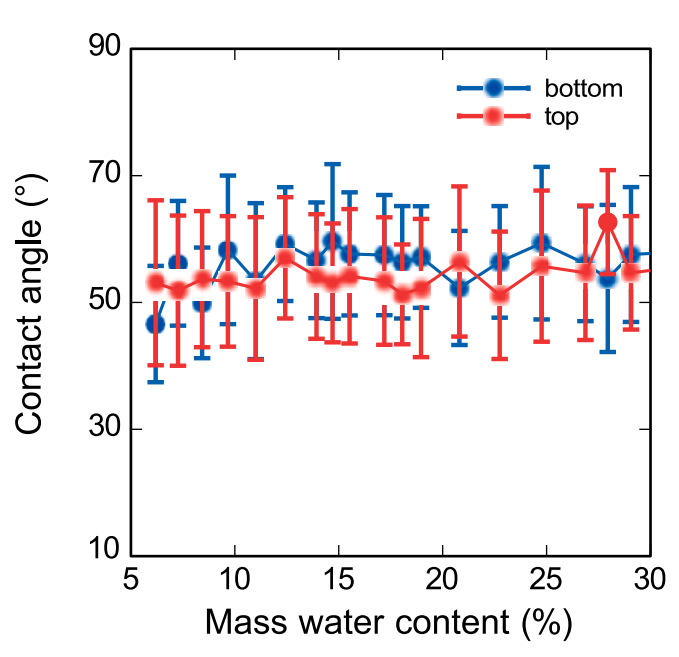


Fig. 14. Variation of the clay water contact angle with the mass water content.

of water at the nanoscale deviates substantially from that of bulk water at the macroscale.

Fig. 9 shows the water number density profiles at various water contents. Despite the different magnitudes of number density, these density curves exhibit a similar mode: the first and second density peaks are located at the distances of 3.75 Å and 6.75 Å from the clay surface (i. e.,  $z_{clay} = \pm 25$  Å), respectively. Further away from the clay surface, water number density gradually decreases. At the center of the clay nanopore (i.e., z=0), the water number density reaches the minimum value. The maximum number density is  $2.36 \times 10^{-2} \mbox{Å}^{-3}$  that is about three times the minimum number density (e.g.,  $0.73 \times 10^{-2} \text{Å}^{-3}$  at  $\theta_g =$ 17.2%). Large number density fluctuations in the vicinity of the claywater interface could indicate a strong effect of soil-water adsorption. It also results in a layered water structure. From the number density profile, the soil water could be partitioned into two parts, e.g., the adsorptive water and the capillary water. The adsorptive water layer extends from the clay surface to the trough after the second peak in the number density profile. The capillary region lies in the remaining pore water space where the capillary effect is dominant. The interfaces between the two regions are approximately located at  $z_{clay} = \pm 16.75 \text{Å}$ from the MD simulation as shown in Fig. 9.

Fig. 10 plots the variation in percentages of adsorptive and capillary water pressures versus mass water content. Table 3 summarizes the percentages of adsorptive and capillary water pressure in the total pore water pressure at different mass water contents. At a low mass water content, e.g.,  $\theta_g=6.2\%$ , the adsorptive water pressure occupies 62.9% of the total pore water pressure. As water content increases, the effect of

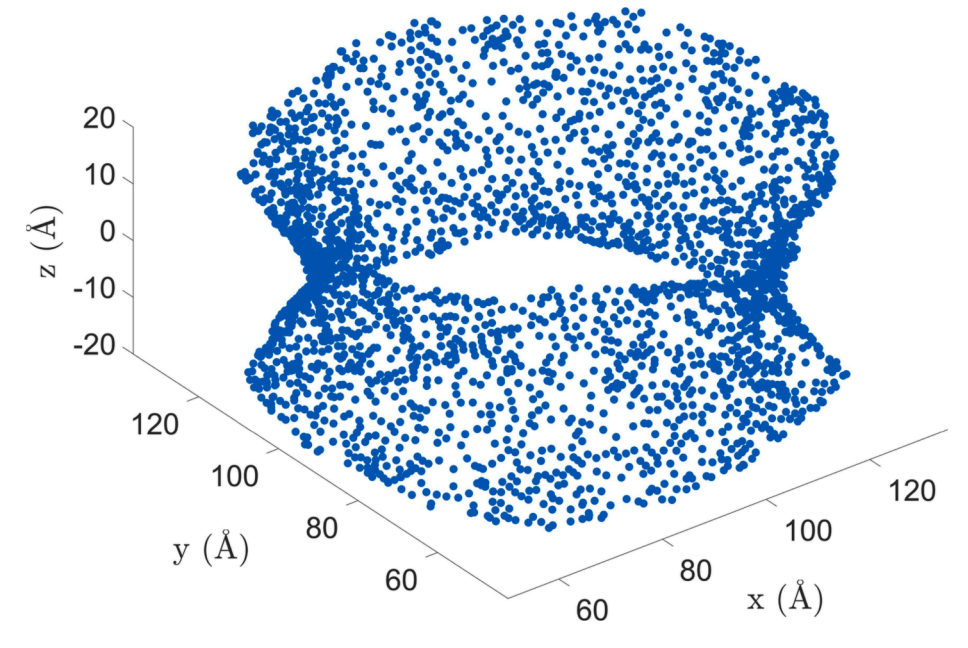


Fig. 15. Schematic representation of the water-air interface.

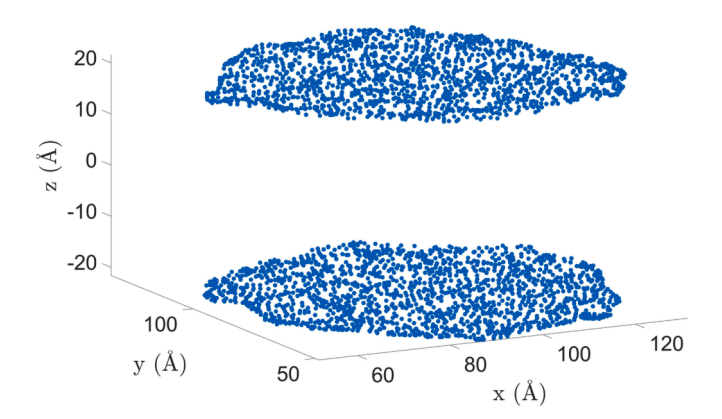
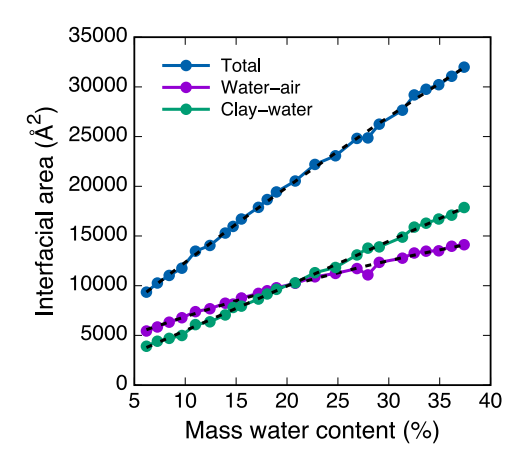


Fig. 16. Schematic representation of the clay-water interface.



**Fig. 17.** Variations of the water–air interface area and the soil–water interface area versus the mass water content.

adsorption is gradually weakened. When the mass water content is around 15%, the effects of adsorption and capillarity are similar. The percentage of adsorptive pressure fluctuates around 45% when mass

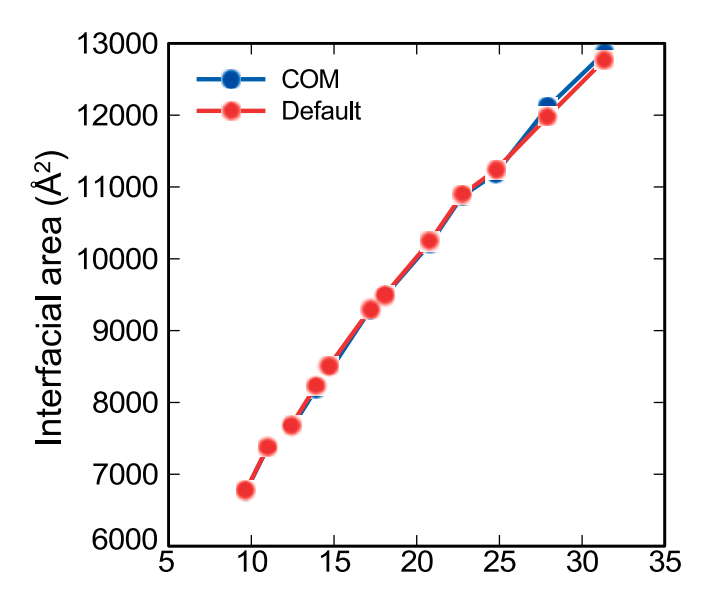


Fig. 18. Comparison of the water—air interface area calculated via the center-of-mass (COM) method and the default water point cloud method.

water content exceeds 20%, and capillarity becomes a dominant factor in the overall negative pore water pressure (i.e., matric suction). The MD results have demonstrated that adsorption plays a significant role in the soil water retention mechanism at a low degree of saturation in clay.

The adsorptive water pressure from our MD simulations was compared to that from an empirical formula (Tuller et al., 1999) that reads

$$\phi_{ads} \approx \phi_{vdW} = \frac{A_H}{6\pi t^3},\tag{7}$$

where  $A_H$  is the Hamaker constant and t is the thickness of adsorptive water layer. For a soil–water system,  $A_H$  is on the order of  $-10\times 10^{-20}$  Joules to  $-10\times 10^{-19}$  Joules. In this study, it was adopted that  $A_H=-6\times 10^{-20}$  Joules. The results in Fig. 9 show that the first non-zero water density occurs near  $z=\pm 22.875 \text{\AA}$ , i.e., 2.125 Å away from the clay surface. The thickness of the adsorptive water layer t is

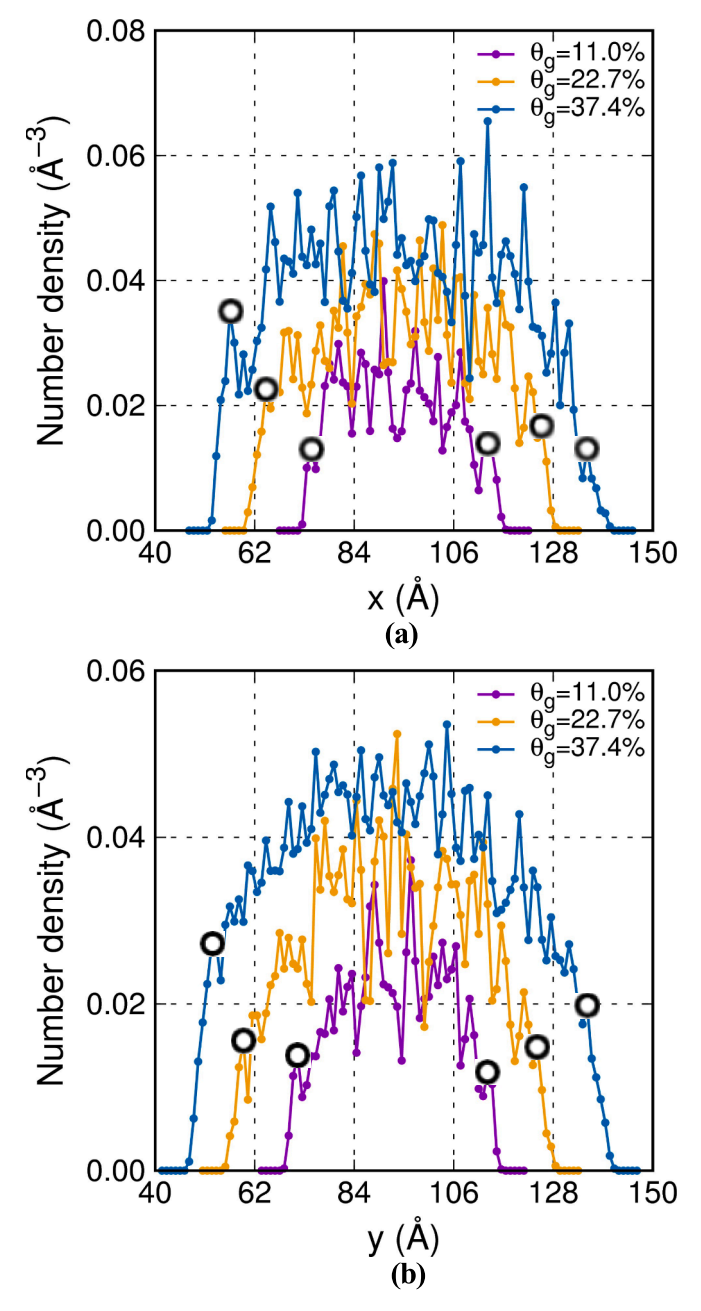


Fig. 19. Water number density at the pore center along (a) the x-direction and (b) y-direction.

approximately 6 Å, e.g., the distance between the trough after the second peak density ( $z=\pm 16.875$ Å) and the outermost water layer ( $z=\pm 22.875$ Å). From equation (7), we have  $f_{ads}=-14.74$  MPa, which is comparable to the adsorptive pressure from our MD results, as illustrated in Fig. 22. We note that it lacks experimental testing data to validate the thickness of the adsorptive water layer assumed in our MD simulations.

The pairwise energy and interaction force between the clay and the adsorptive water layer can be used to describe clay-water interactions. Pairwise energy includes the van der Waals component and the longrange Coulombic component. Since only adsorptive water is included, this energy term specifically refers to sorptive energy. Table 4 summarizes the sorptive energy between clay and adsorptive water at different mass water contents. As the mass water content increases from 9.7% to 34.9%, the magnitude of sorptive energy increases by 170% due to increased adsorptive interactions. Fig. 11 plots the variation of

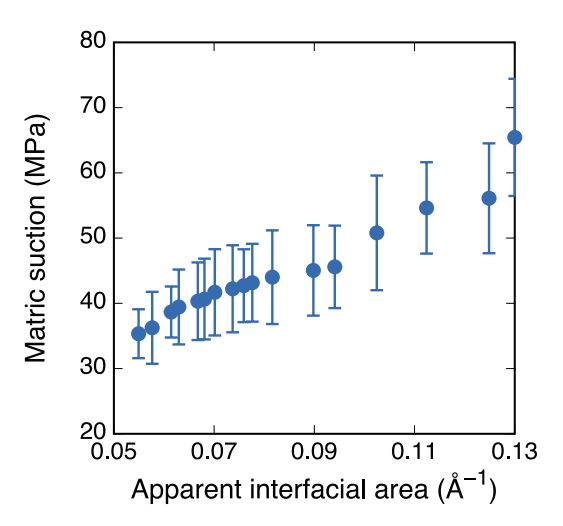


Fig. 20. Matric suction versus the apparent water-air interfacial area.

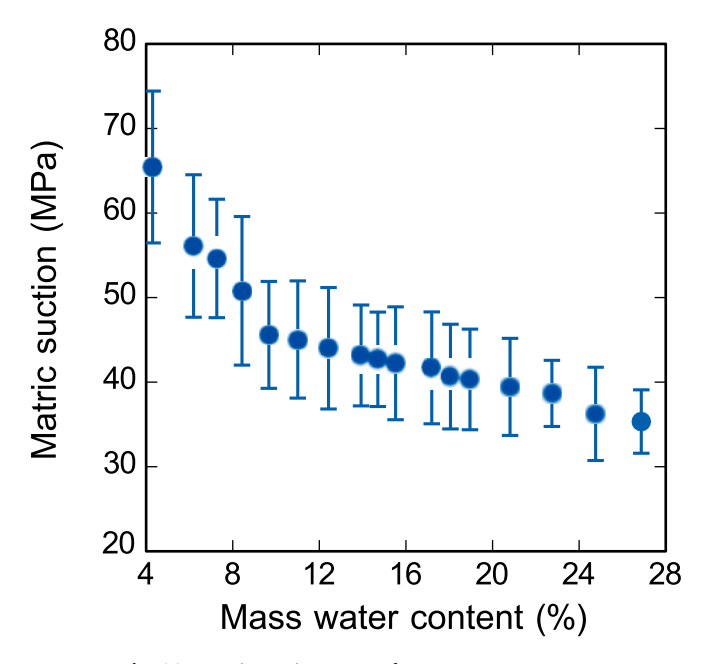


Fig. 21. Matric suction versus the mass water content.

interaction force with the mass water content. The increase in the adsorptive force is mainly due to the increase of accumulated water molecules in the adsorptive water layer during the wetting process (i.e., increasing water in the pore space).

## 3.2. Area and thickness of the water-air interface at various mass water contents

Fig. 12 shows a soil -water retention surface in terms of generalized matric suction  $(\phi_m)$ , mass water content  $(\theta_g)$ , and apparent water–air interface area  $(A_a)$  through a standard curve fitting technique. The water–air interface area was computed through the method introduced in the previous section. Fig. 13 shows the water point clouds for 6 simulations. Since clay particles were fixed, the height of soil water remains almost unchanged  $(h_w=43.5\pm0.1~\text{Å})$  and the soil water body expands along the radial direction with increasing mass water content. We further demonstrate that the mass water contents have a mild effect on the shape of the water meniscus through the contact angle. The contact angle was computed using the method proposed in Song and Zhang (2021).

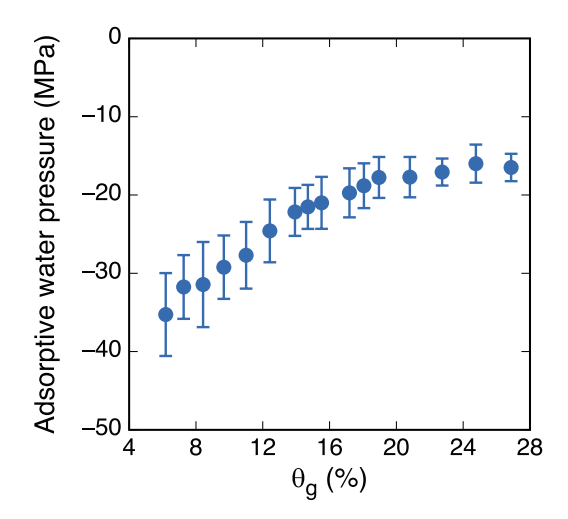


Fig. 22. Adsorptive water pressure versus the mass water content and the apparent interfacial area.

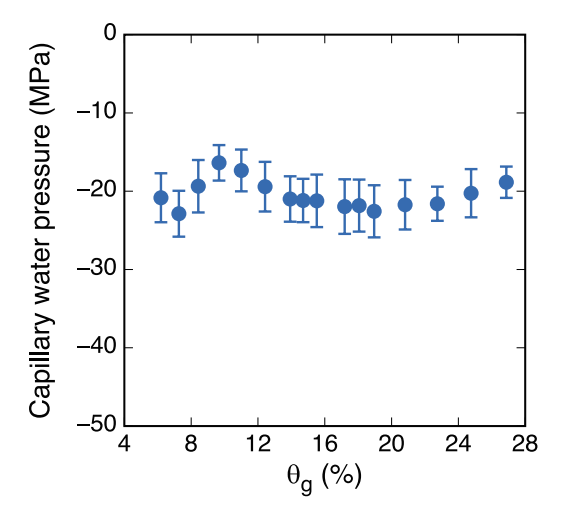


Fig. 23. Capillary water pressure versus the mass water content and the apparent interfacial area.

Fig. 14 plots the variation of the clay-water contact angle with respect to the mass water content. In Fig. 14 "top" and "bot" denote the top and bottom clay-water interfaces, respectively. From the results in Fig. 14 it can be postulated that the shape of the water meniscus is almost identical at the different degrees of saturation due to the fixed pore space.

Figs. 15 and 16 present the schematic of the water–air interface and the clay-water interface, respectively. Fig. 17 plots the water–air interface area versus water mass content. For comparison, the total interface area (i.e., summation of the water–air interface area and the water-soil interface area) and the water-soil interface area are also plotted. The total interface area increases from 9350 Ų to 31984 Ų as the mass water content varies from 6.2% to 37.4%. Both the water–air interface area and the clay-water interface area show a nearly linear increase with respect to the mass water content. It can be found that the clay-water interfacial area has a relatively larger growth rate than the water–air interface area with respect to the mass water content. The two curves for the water–air and clay-water interface areas intercept at around  $\theta_{\rm g}=20\%$ .

The efficacy of the center-of-mass (COM) method in the surface area calculation was evaluated by comparing the results with the ones from the original (default) water point cloud. The major difference between the two methods is the total number of points in the point cloud. In the default water point cloud, the total number of points is  $3N_w$ , and each atom determines the coordinate of the corresponding point. In the center-of-mass implementation, the total number of points is  $N_w$ . Fig. 18 compares the water–air interface area calculated from the COM-based point cloud and the default point cloud. The deviation is less than 0.1% for all mass water contents.

The thickness of the water–air interface is an important physical property of water–air interface (Fredlund, 2006). Based on our MD simulations, we could determine the interface thickness from the number density distribution of water in the middle plane of the clay pore. The water between the planes that are parallel to the clay surface at z = -0.5 Å and z = 0.5 Å were collected and analyzed to avoid the effect of water-clay interactions. Fig. 19 presents the number density distribution of water at the pore center along the x and y directions. It can be found that the water number density increases sharply from zero to a peak value near the clay surface. The first density peak is marked with a black circle in Fig. 19. For example, a density jump up to 0.036 Å<sup>-3</sup> can be seen within a distance of  $\Delta x = 5$  Å at  $\theta_g = 37.4\%$ . Since water density shows a significant change across the water–air interface, we assume that the thickness of the water–air interface is equal to the distance between the outermost water layer and the first density peak. Based on

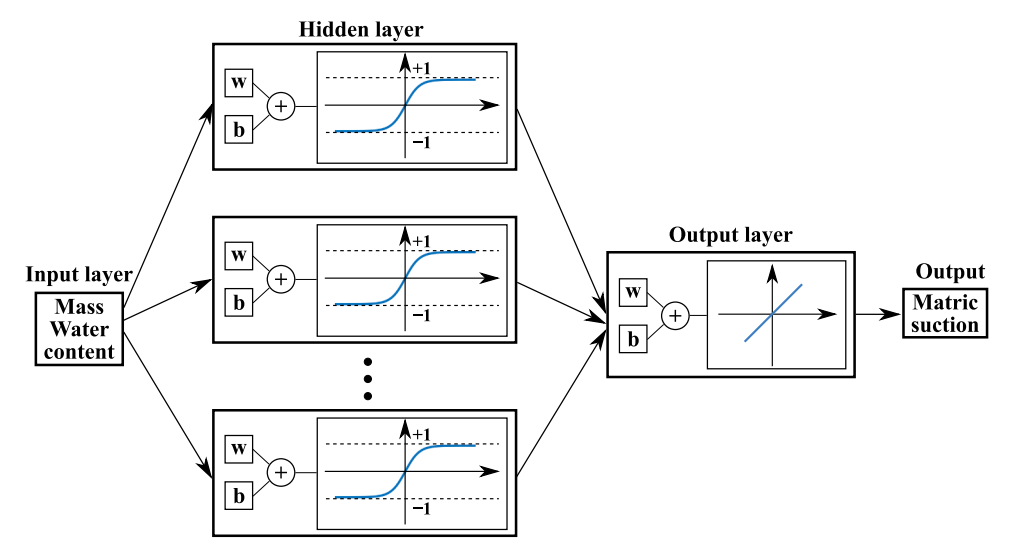


Fig. 24. Architecture of the feed-forward neural network.

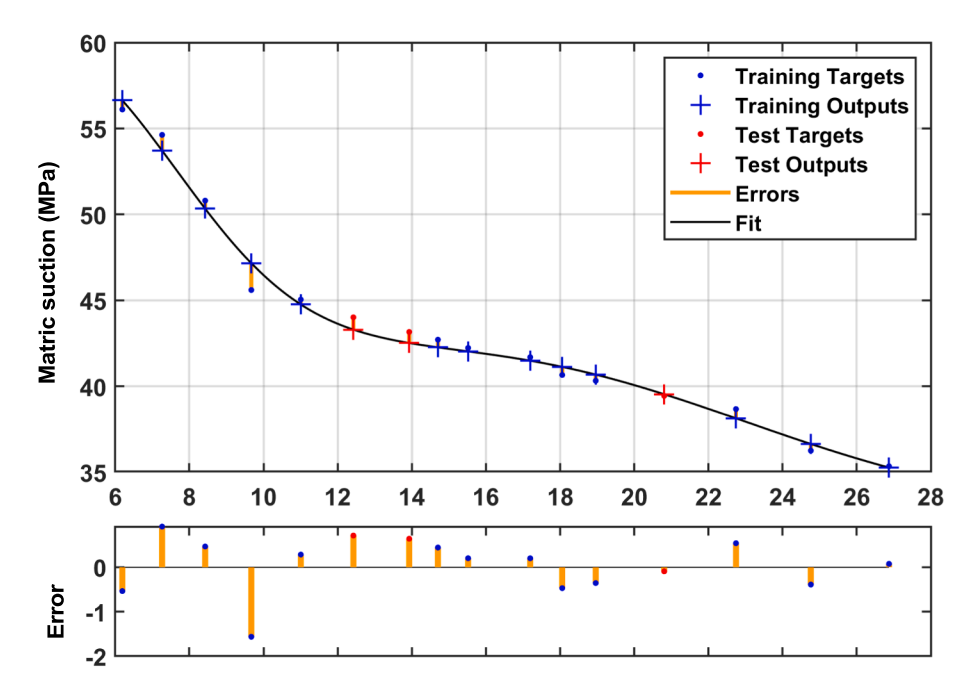


Fig. 25. Variation of matric suction versus the mass water content through FNN.

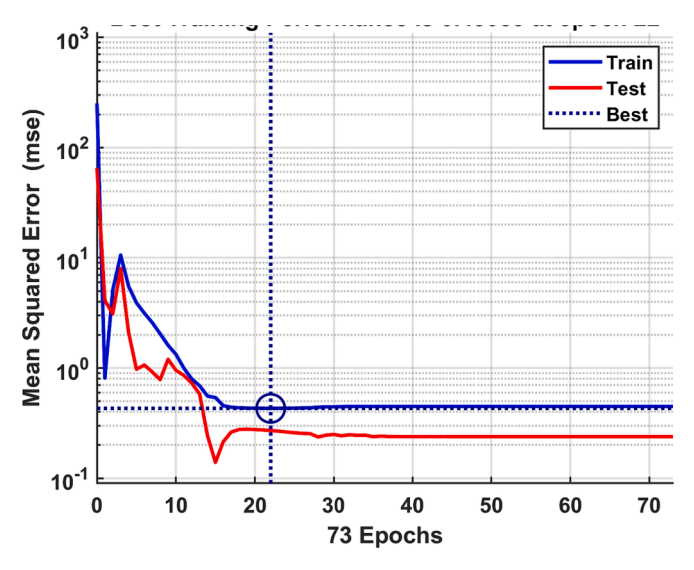
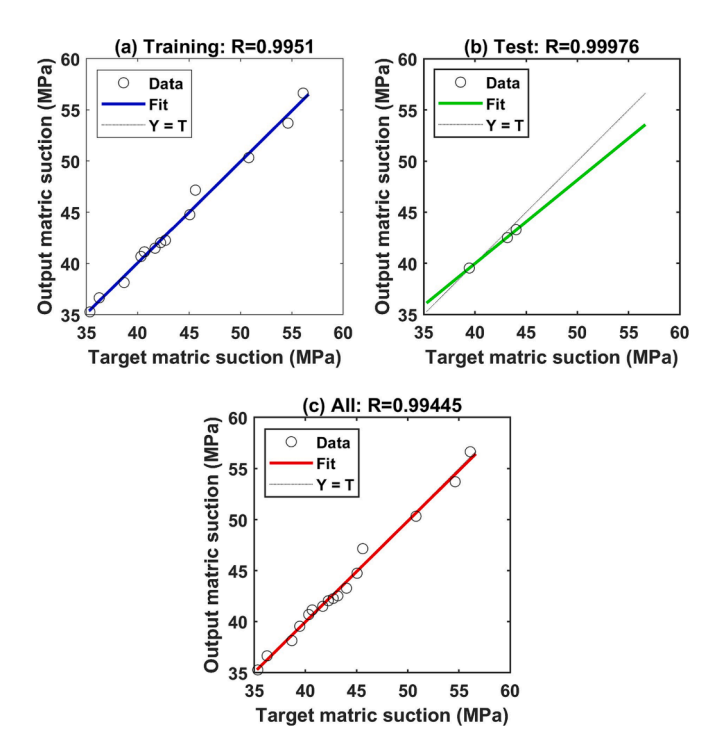


Fig. 26. Performance of the training for the relation bewteen matric suction and the mass water content.

this assumption, the values of interfacial thickness at the mass water contents of 11.0%, 22.7%, and 37.4% are 5 Å, 5.5 Å, and 5.75 Å, respectively. Previous studies have shown that the thickness of the water–air interface is on the order of 1.5–2 water molecular diameters, e.g., approximately 5 Å (Townsend and Rice, 1991; Fredlund and Rahardjo, 1993; Israelachvili, 2015). This consistency could imply that the water number density from our MD simulations is viable in determining the thickness of the water–air interface in unsaturated clay.

#### 3.3. Soil-water retention curves through neural networks

In this section, the results of our MD simulations were analyzed to distinguish adsorption and capillarity in the soil–water retention mechanism. We investigate the relation between matric suction and mass water contents through a neural network (Goodfellow et al., 2016). We first present the results from the MD simulations. Fig. 20 plots the



**Fig. 27.** Plot of the regression during training for the curve of matric suction versus the mass water content.

variation of matric suction with the apparent interfacial area. The dot represents the mean value, and the error bar represents the standard deviation. Note that the same notations apply to the following figures. In general, matric suction increases with the apparent interfacial area. Here, the apparent water—air interfacial area is defined as the water—air interfacial area per water volume. The experimental data on the water—air interfacial area at the nanoscale is not available in the literature. It is noted that the  $A_\alpha - \theta_g$  relationship obtained from our MD simulations follows the general trend as shown in the results of laboratory tests at the continuum scale (Costanza-Robinson and Brusseau,

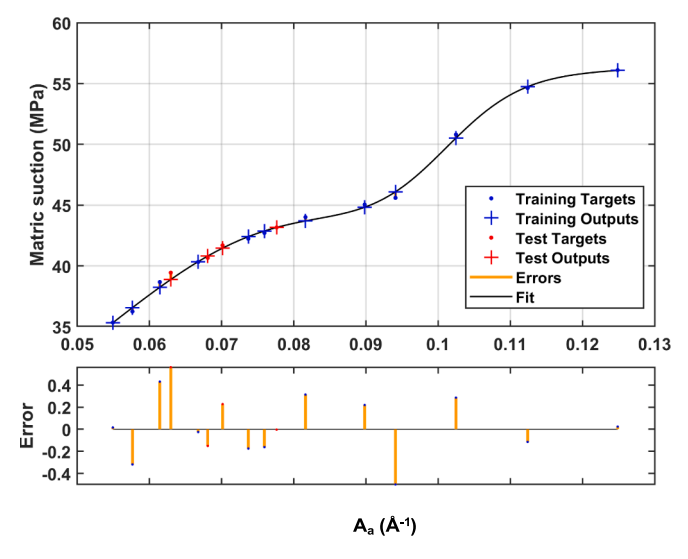
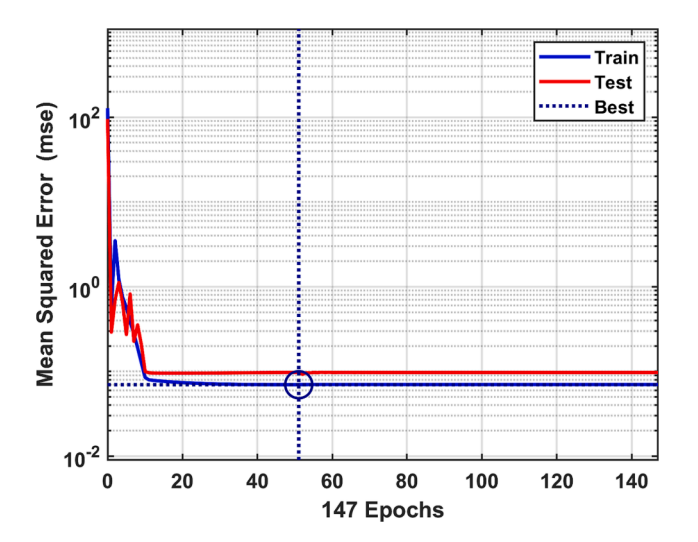


Fig. 28. Plot of the variation of matric suction versus the apparent interfacial area through FNN.



**Fig. 29.** Performance of the training for the curve of matric suction versus the apparent interfacial area.

2002). Fig. 21 plots the variation of matric suction with the mass water content. The results in Fig. 21 show that as the mass water content increases from 4.30% to 26.87%, matric suction decreases from 65.4 MPa to 35.86 MPa. Matric suction drops faster as the mass water content is less than 10 %. As the mass water content is greater than 10 %, the decreasing rate of matric suction is lower. Adsorptive water pressure and capillary pressure can be distinguished based on the water density distribution. Fig. 22 presents the adsorptive water pressure with the mass water content, the lower the absolute value of adsorptive water pressure. Fig. 23 presents the capillary water pressure with the mass water content. The results show that the capillary water pressure oscillates at the average value of  $-20.71\pm1.9$  MPa. These results are corroborated by the slight variations of contact angles of the clay-water systems at different water contents (See Fig. 14).

Next, we apply a neural-network deep learning model to predict the relationship between matric suction, the mass water content, and the apparent interfacial area. Given the input (e.g., mass water contents) and the corresponding output (e.g., matric suction), the neural network can generate a model function without any preliminary knowledge

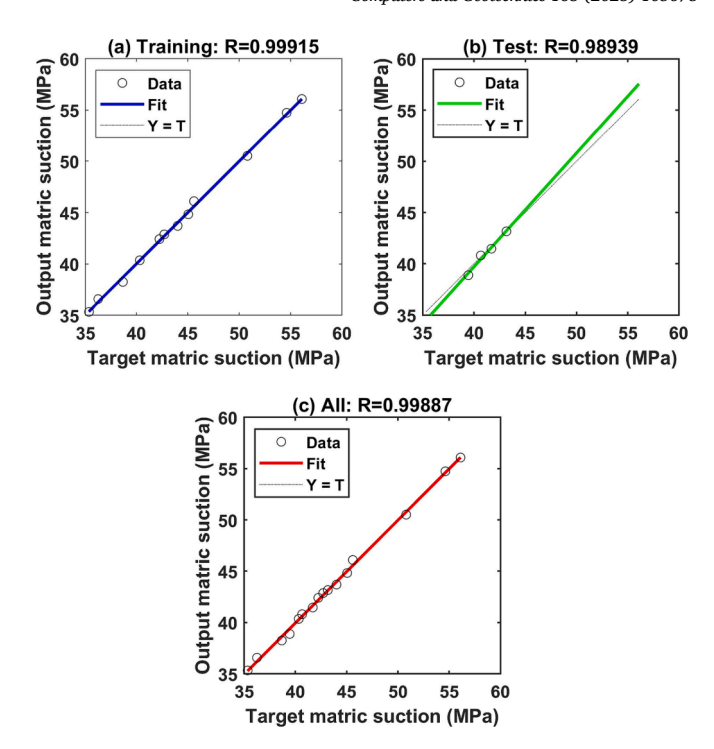


**Fig. 30.** Plot of the regression during the training for the relationship between matric suction and the apparent interfacial area.

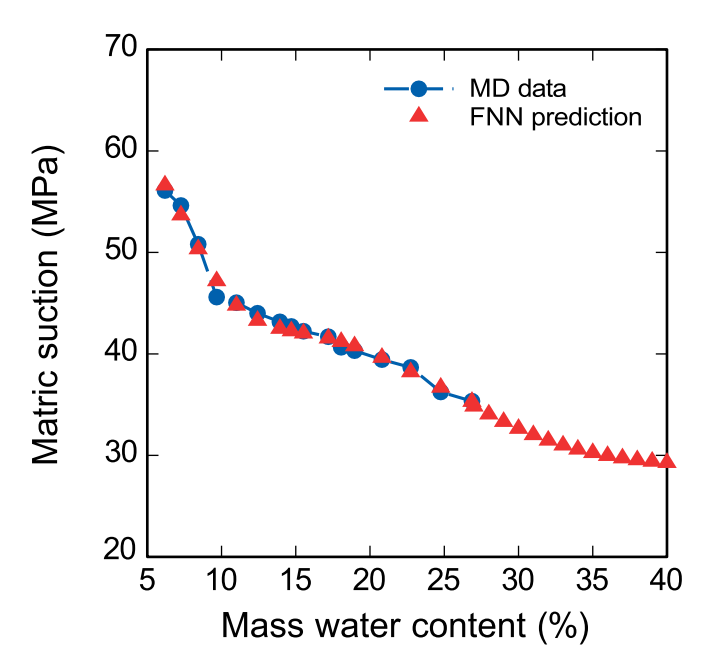
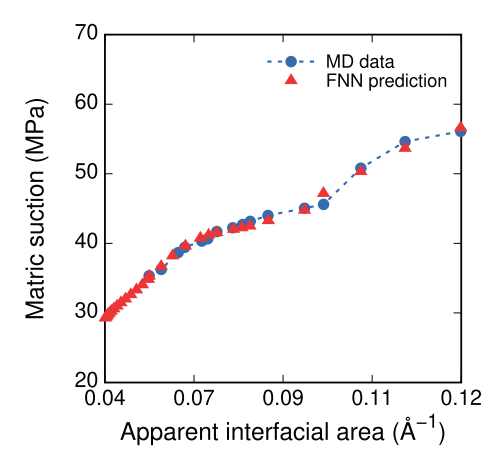


Fig. 31. Variation of matric suction with the mass water content from the MD results and the trained FNN.

about the structure of the function. This is the fundamental difference from the traditional curve fitting of known model functions such as polynomial and power functions. In what follows, we briefly introduce the neural network designed for this study. Fig. 24 plots the architecture of the feed-forward neural network (FNN) adopted in this study. With hidden sigmoid neurons and linear output neurons, the neural network allows for fitting 2-dimensional mapping problems. The neural network is trained with the Bayesian regularization algorithm. Therefore, the neural network adopted is named by Bayesian regularized feed-forward neural network (BRFNN). Bayesian regularization is a mathematical



**Fig. 32.** Variation of matric suction with the apparent interfacial area from the MD results and the trained FNN.

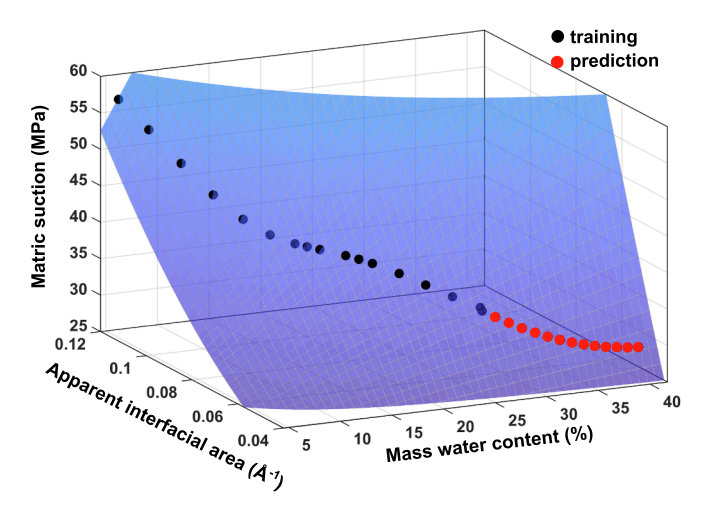


Fig. 33. Relationship among matric suction, the mass water content, and the apparent interfacial area.

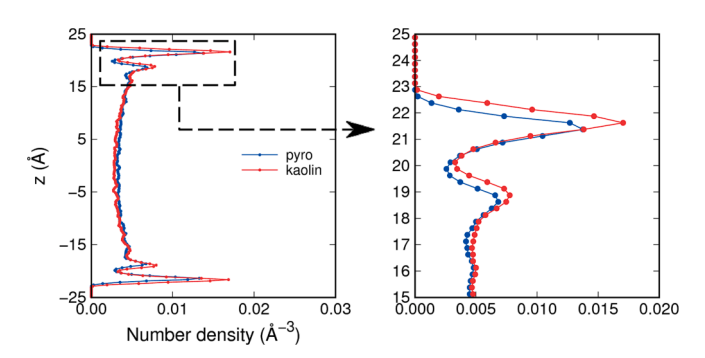


Fig. 34. Number density of the water oxygen in the clay pore.

process that converts a nonlinear regression into a "well-posed" statistical problem (MacKay, 1992). The initial weights are assigned by the algorithm in (Nguyen and Widrow, 1990), and the optimization is performed by the Gauss-Newton algorithm (Foresee and Hagan, 1997). The Bayesian regularization approach involves the probability distribution of neuron network weights, which differs from conventional network training algorithms (i.e., the optimal weight set chosen by minimizing the error function).

Thus, the network predictions are in the form of a probability distribution. The salient feature of BRFNN is that the validation process is

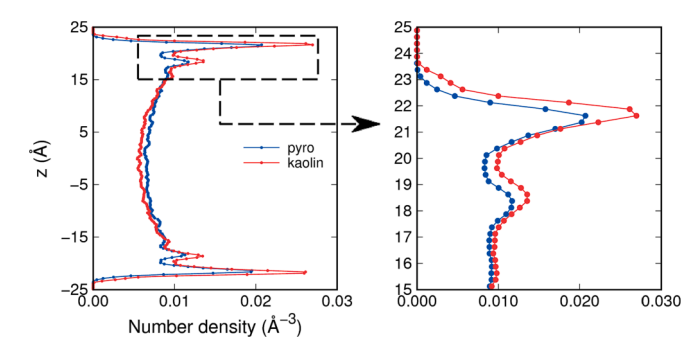


Fig. 35. Number density of the water hydrogen in the clay pore.

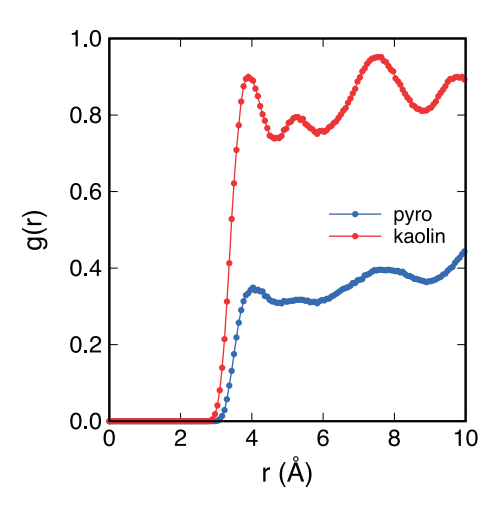


Fig. 36. Radial distribution function of the atom pair Oc-Ow near the clay surface.

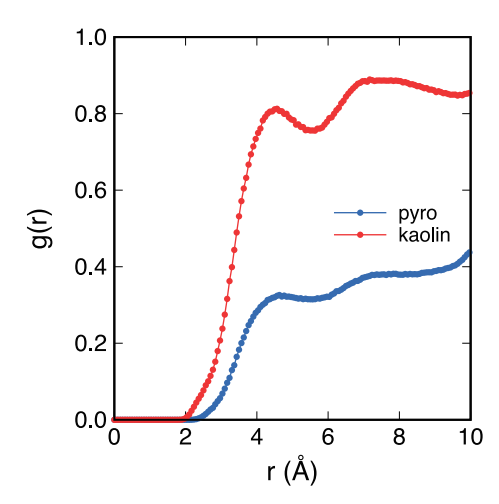


Fig. 37. Radial distribution function of the atom pair Oc-Hw near the clay surface.

not needed (Burden and Winkler, 2009). The input of the neural network is the vector of mass water content. Once received by the hidden layer and multiplication, they are passed to the neurons of the output layer. In the hidden layer, a neuron first computes the weighted sum of input vectors. Then, a constant bias is added to the weighted sum. Finally, the value is fed into the activation function to obtain the output. In the backpropagation, the cost function  $\it E$  to be minimized is

$$E = \mu E_D + \nu E_W, \tag{8}$$

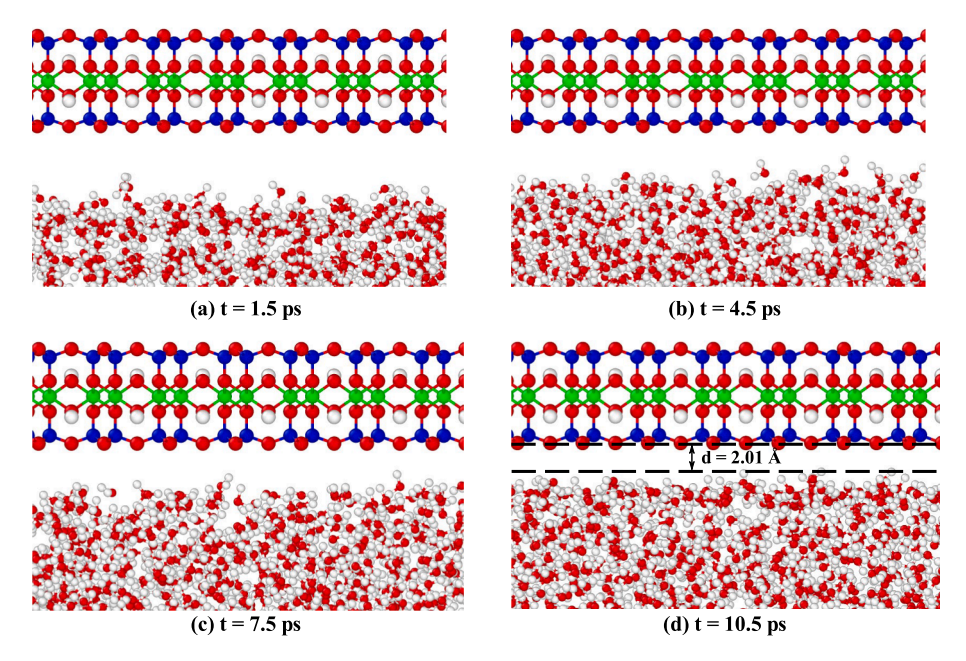


Fig. 38. Snapshots of the water molecules in the pyrophyllite pore.

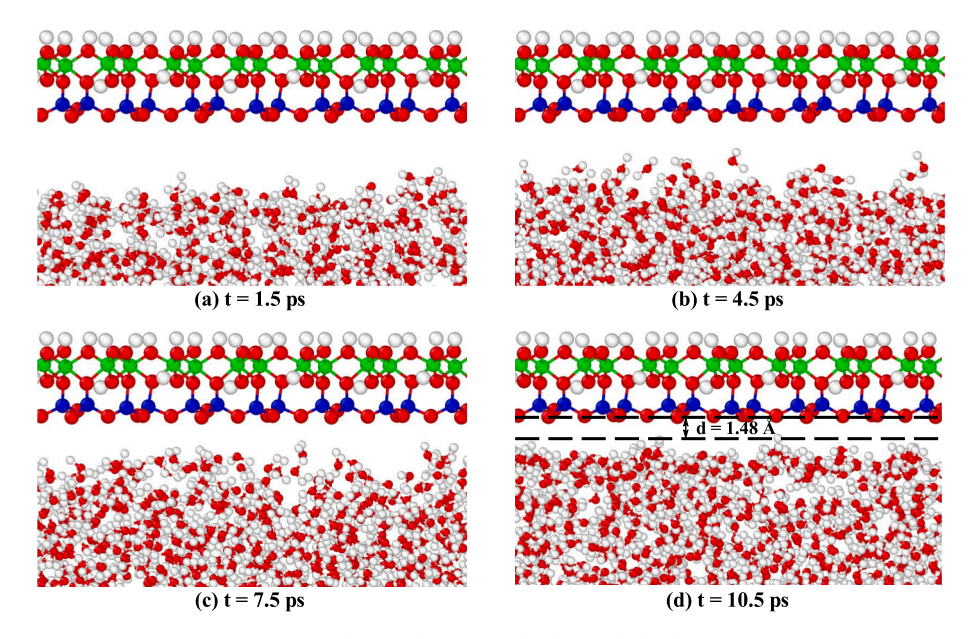


Fig. 39. Snapshots of the water molecules in the kaolinite pore.

where  $\mu$  and  $\eta$  are hyperparameters,  $E_D$  is the sum of squared errors, and  $E_W$  is the error of the weights. The sum of squared errors reads

$$E_D = \sum_{i=1}^{N_D} (y_i - \hat{y}_i)^2, \hat{y}_i = \sum_{j=1}^{N_N} F_{act}(w_j x_i + b_j),$$
 (9)

where  $N_D$  is the dimensions of the input vector,  $y_i$  is the target value (e.g., matric suction),  $\widehat{y}_i$  is the predicted value (e.g., matric suction) as a function of the input value  $x_i$  (e.g., mass water content),  $N_N$  is the number of neurons,  $w_j$  and  $b_j$  are the weight and bias corresponding to the j-th neuron, respectively, and  $F_{act}$  is the activation function in the form of a hyperbolic tangent sigmoid (Vogl et al., 1988). The error of weights  $E_W$  is written as

$$E_W = \sum_{j=1}^{N_N} w_j^2. {10}$$

The input vector of the mass water content and the target vector of matric suction are randomly divided into two groups. For instance, 75% of the input data was used for training, and 25% of the input data was used as an independent test of the neural network generalization.

Fig. 25 plots the output and target values of matric suction during training and testing and the errors. Fig. 26 plots the mean squared error (MSE) variation versus the number of epochs for the training and test data. Here MSE measures the average squared difference between the predicted values of matric suction and the actual values from MD simulations. The number of epochs is a hyperparameter. An epoch is when all the training data is used at once and is defined as the total number of iterations of all the training data in one cycle for training the machine learning model. As shown in Fig. 26, the MSE drops significantly with the initial increase of the epoch number. After the oscillation around epoch 4, the mean squared error continues to decrease. The best training performance is 0.43053 at epoch 22. Fig. 27 plots the linear regression

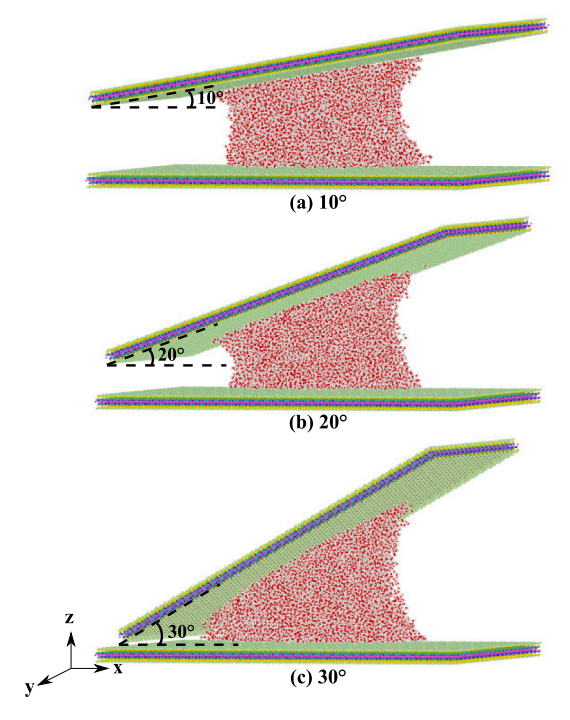


**Fig. 40.** Clay-water models with the two clay particles aligned with an angle at (a)  $10^{\circ}$ , (b)  $20^{\circ}$ , and (c)  $30^{\circ}$ .

**Table 5**Percentages of the soil–water interface area and the air–water interface area for the three angled clay particle configurations.

Angle between two clay particles (°)	Clay-water area (%)	Air-water area (%)
10	48.5	51.5
20	50.0	50.0
30	55.0	45.0

**Table 6**Percentages of the adsorptive water pressure and the capillary water pressure under three clay particle configurations.

Angle between two clay particles (°)	Adsorptive water pressure (%)	Capillarity water pressure (%)
10	46.4	53.6
20	46.0	54.0
30	47.5	52.5

**Table 7**Summary of matric suctions and water–air interface areas for three pore widths under the same water mass content.

Pore width (nm)	Matric suction (MPa)	Water-air interface area ( $\mathring{A}^2$ )
4	$46.4 \pm 5.69$	7659
5	$42.23 \pm 6.68$	8762
6	$39.06 \pm 4.09$	9930

coefficient R between the target matric suction and the predicted matric suction for (a) training, (b) test, and (c) the whole dataset. The regression values of the training phase (R = 0.9951) and the test phase (R = 0.99976) indicate a good match between the target and the model output.

Fig. 28 plots the predicted and the target matric suction during training and testing, given the input of the apparent interfacial area. Fig. 29 shows the variation of mean squared errors with the epoch

number. The results indicate that the best performance is 0.06977, obtained at epoch 51. Fig. 30 plots the linear regression coefficient R between the target and the predicted matric suction during (a) training, (b) test, and (c) the total dataset. The regression values of the training phase (R = 0.99915) and the test phase (R = 0.98939) indicate a good fit between the target and the model output.

Furthermore, we use the trained model to predict matric suction and the apparent interfacial area at mass water contents outside the range of the trained data. Fig. 31 shows the variation of matric suction with the mass water content. Fig. 32 plots the variation of matric suction and the apparent interfacial area. Combining the results in Figs. 31 and 32, Fig. 33 presents the relation among matric suction, the mass water content, and the apparent interfacial area. Overall, the results show that neural-networks-based machine learning is a useful tool to analyze the MD results that explicitly consider the soil–water adsorption and generate the soil–water retention curves without prescribing a specific functional relationship between matric suction, the water mass content, and the apparent interfacial area.

#### 4. Discussions

In this section, we first present the water adsorptive mechanisms in pyrophyllite and kaolinite through density functions, radial distribution functions, and water molecule orientations on the clay surface. Then we discuss the effect of clay particle configurations and pore geometrical sizes on the clay-water adsorption mechanism at the nanoscale through MD simulations with different clay particle configurations and pore geometrical dimensions.

#### 4.1. Clay mineral types

It is known that clay mineral types impact the clay-water adsorption mechanism. We compare the water adsorption mechanism between kaolinite and pyrophyllite at the atomic scale. Kaolinite is a 1:1 type clay mineral. The primary water adsorption mechanism of kaolinite is surface hydroxyl hydration. For comparison, we construct an unsaturated kaolinite-water model with the exact dimensions of the pyrophyllitewater model in Section 2. The mass water content is assumed 22.741%. Figs. 34 and 35 compare the number densities of water oxygen and water hydrogen in the pyrophyllite pore and the kaolinite pore, respectively. The larger peak density and shorter distance from the first peak to the clay surface demonstrate that kaolinite has a greater water adsorption capacity. This is corroborated by the larger matric suction in the kaolinite-water model than that in the pyrophyllite-water model, i. e., 49.50 MPa versus 38.67 MPa. The radial distribution function (RDF) is used to detect the location of the adsorptive water layer. Figs. 36 and 37 plot the RDF of the atom pairs Oc-Ow (i.e., clay tetrahedral oxygenwater oxygen) and Oc-Hw (i.e., clay tetrahedral oxygen-water hydrogen) near the two clay surfaces, respectively. The results show that the larger RDF of water in the kaolinite pore implies greater water absorption at the kaolinite surface. For instance, the distance between the first peak of RDF to the kaolinite surface is about 4 Å which agrees with the location of the first peak water number density as shown in Figs. 34 and 35.

Furthermore, the snapshots of the MD simulations are presented to show the water molecular distribution due to adsorption at the two clay surfaces. Figs. 38 and 39 show the snapshots of the water molecule in the pyrophyllite and kaolinite pores during the adsorptive process at different run times, respectively. The results show that the water molecules move closer to the clay surface and exhibit orientation in both clay pores from 1.5 ps to 10.5 ps due to adsorption. The difference is the distance between the closest water molecule layer to the clay surface. The distances are 1.48 Å for the kaolinite platelet and 2.01 Å for the pyrophyllite platelet, which indicates the difference in water adsorption mechanisms and adsorption strength between kaolinite and pyrophyllite.

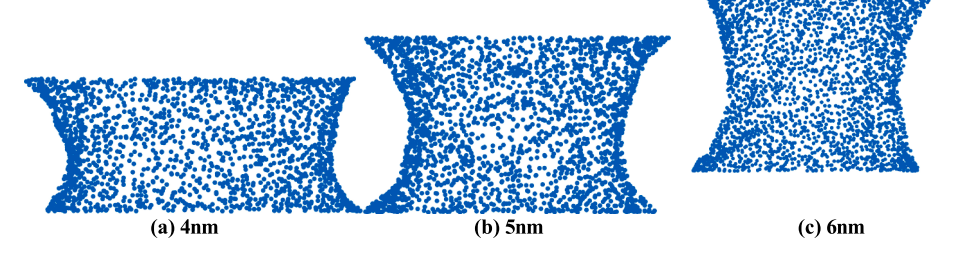


Fig. 41. Configurations of equilibrated soil water in the clay pore of width: (a) 4 nm, (b) 5 nm, and (c) 6 nm.

#### 4.2. Clay particle configurations

The configuration of the two clay platelets could affect the soil water retention mechanism. To study the effect of clay platelet configurations on soil water retention, we simulated three cases where two clay particles are aligned with angles of 10°, 20°, and 30°, respectively. The three configurations are denoted by cases 1, 2, and 3, respectively. The center-to-center distance between the two clay particles remains the same, i.e., 5 nm. The mass water content is 31.3% for each case. Due to the particle rotation, the dimension of the simulation box in the zdimension is increased as well. The equilibrated configurations are shown in Fig. 40. Using the alpha- shape method, we computed the water-air interface area for the three cases. The total interface areas, i.e., the summation of the soil-water interface area and the air-water interface area, are approximately 28338 Å<sup>2</sup>, 28242 Å<sup>2</sup>, and 29035 Å<sup>2</sup>, respectively. Table 5 summarizes the percentages of the soil-water interface area and the air-water interface area for the three angled clay particle configurations. MD results show that the soil-water model with a larger angle between the two clay particles generates larger matric suction. The matric suctions for cases 1, 2, and 3 are  $37.19 \pm 5.57$  MPa,  $39.75 \pm 4.74$  MPa,  $45.83 \pm 3.24$  MPa, respectively. Table 6 compares the percentages of the adsorptive water pressure and the capillary water pressure under the three clay particle configurations. Thus, the adsorptive water pressures under the three configurations are  $-17.26\ \pm$ 2.59 MPa,  $-18.30 \pm 2.18$  MPa, and  $-21.75 \pm 1.54$  MPa, respectively.

#### 4.3. Effect of the pore width

In this part, we investigate the effect of pore widths, i.e., the distance between the two clay particles, on matric suction and the interfacial area. We compare the results from the three pore widths, i.e., 4 nm, 5 nm, and 6 nm, under the mass water content of 15.1%. Table 7 summarizes the results. It is found that the matric suction decreases with increasing pore width. This is partially due to the reduced capillary force with increasing pore width. The water—air interface area rises with the pore width. To interpret this, we compare the point clouds of soil water molecules for the three cases, as shown in Fig. 41. The radii of the claywater interface are 7.9 nm, 7.4 nm, and 6.9 nm for the three pores, respectively. However, the change in the pore width might be a dominant factor in that the case for a larger width generates a larger water—air interface area under the same conditions.

#### 5. Concluding remarks

We have conducted MD simulations to investigate the soil—water adsorptive and capillary mechanisms of unsaturated clay. The MD model consists of two parallel clay plates and water confined in the clay nanopore. MD simulations were performed at low mass water contents. For processing the MD results, soil water was represented by a point cloud through the center-of-mass method. The water—air interfacial area was calculated using the alpha-shape method. Adsorption was explicitly considered by distinguishing adsorptive pressure from capillary pressure. We have characterized the adsorptive water layer based on the water density profile. The thickness of the adsorptive water layer and

the adsorptive water pressure from our MD results are consistent with the results in the literature. For the first time, the feed-forward neural network that does not require a prior function was utilized to generate the nanoscale soil—water retention curve in terms of matric suction, the mass water content, and the apparent interfacial area. The application of the trained neural network was demonstrated by predicting matric suction beyond the range of trained mass water contents. The MD results have demonstrated that adsorption is a dominant mechanism of the nanoscale soil water retention under a low mass water content. For instance, the adsorptive water pressure accounts for more than 60% of the total pore-water pressure at the low mass water content in this study. We note that the study in this article is limited to the pore between two clay particles. The assemblage of clay particles should be considered to study the nanoscale clay-water retention mechanism through MD, which is ongoing research and will be reported in a future publication.

#### CRediT authorship contribution statement

**Zhe Zhang:** Conceptualization, Methodology, Investigation, Writing – original draft. **Xiaoyu Song:** Supervision, Conceptualization, Methodology, Investigation, Writing – review & editing.

#### **Declaration of Competing Interest**

The authors declare that they have no known competing financial interests or personal relationships that could have appeared to influence the work reported in this paper.

#### Data availability

Data will be made available on request.

#### Acknowledgments

This work has been supported in part by the US National Science Foundation under contract numbers 1659932 and 1944009. The support is gratefully acknowledged. Any opinions or positions expressed in this article are those of the authors only and do not reflect any opinions or positions of the NSF.

#### References

Allen, M.P., Tildesley, D.J., 2017. Computer simulation of liquids. Oxford University Press.

Alonso, E.E., 2021. Triggering and motion of landslides. Geotechnique 71 (1), 3–59.
 Alonso, E.E., Gens, A., Josa, A., 1990. A constitutive model for partially saturated soils.
 Geotechnique 40 (3), 405–430.

Alonso, E.E., Pereira, J.-M., Vaunat, J., Olivella, S., 2010. A microstructurally based effective stress for unsaturated soils. Geotechnique 60 (12), 913–925.

Amarasinghe, P.M., Anandarajah, A., Ghosh, P., 2014. Molecular dynamic study of capillary forces on clay particles. Appl. Clay Sci. 88, 170–177.

Barber, C.B., Dobkin, D.P., Huhdanpaa, H., 1996. The quickhull algorithm for convex hulls. ACM Transactions on Mathematical Software (TOMS) 22 (4), 469–483.Berendsen, H., Grigera, J., Straatsma, T., 1987. The missing term in effective pair potentials. J. Phys. Chem. 91 (24), 6269–6271.

Boissonnat, J.-D., 1984. Geometric structures for three-dimensional shape representation. ACM Transactions on Graphics (TOG) 3 (4), 266–286.

- Borja, R.I., 2004. Cam-clay plasticity. part v: A mathematical framework for three-phase deformation and strain localization analyses of partially saturated porous media. Comput. Methods Appl. Mech. Eng. 193 (48–51), 5301–5338.
- Borja, R.I., 2006. On the mechanical energy and effective stress in saturated and unsaturated porous continua. Int. J. Solids Struct. 43 (6), 1764–1786.
- Botan, A., Rotenberg, B., Marry, V., Turq, P., Noetinger, B., 2011. Hydrodynamics in clay nanopores. J. Phys. Chem. C 115 (32), 16109–16115.
- Brooks, R.H., 1965. Hydraulic properties of porous media. Colorado State University.
- Brooks, B. R., Bruccoleri, R. E., Olafson, B. D., States, D. J., Swaminathan, S. a., and Karplus, M. (1983) Charmm: a program for macromolecular energy, minimization, and dynamics calculations. Journal of computational chemistry, 4(2):187–217.
- Brusseau, M.L., Peng, S., Schnaar, G., Murao, A., 2007. Measuring air- water interfacial areas with x-ray microtomography and interfacial partitioning tracer tests. Environ. Sci. Tech. 41 (6), 1956–1961.
- Burden, F., Winkler, D., 2009. Bayesian regularization of neural networks. Artificial neural networks: methods and applications 23–42.
- Butt, H.-J., Graf, K., Kappl, M., 2013. Physics and chemistry of interfaces. John Wiley & Sons.
- Cao, J., Jung, J., Song, X., Bate, B., 2018. On the soil water characteristic curves of poorly graded granular materials in aqueous polymer solutions. Acta Geotech. 13, 103–116.
- Chen, Z., Cao, J., Bate, B., and Song, X. (2019). Reply to "discussion of on the soil water characteristic curves of poorly graded granular materials in aqueous polymer solutions' by junnan cao, jongwon jung, xiaoyu song and bate bate, acta geotechnica, 2018, 13 (1): 103–116" by peng liu and xiaoming liu. Acta Geotechnica, 14: 577–578.
- Chen, L., Kibbey, T.C., 2006. Measurement of air- water interfacial area for multiple hysteretic drainage curves in an unsaturated fine sand. Langmuir 22 (16), 6874-6880
- Clausius, R., 1870. Xvi. on a mechanical theorem applicable to heat. The London, Edinburgh, and Dublin Philosophical Magazine and Journal of. Science 40 (265), 122–127.
- Costanza-Robinson, M.S., Brusseau, M.L., 2002. Air-water interfacial areas in unsaturated soils: Evaluation of interfacial domains. Water Resour. Res. 38 (10), 13–111.
- Cygan, R.T., Liang, J.-J., Kalinichev, A.G., 2004. Molecular models of hydroxide, oxyhydroxide, and clay phases and the development of a general force field. J. Phys. Chem. B 108 (4), 1255–1266.
- Edelsbrunner, H. and Mucke, E. P. (1994). Three-dimensional alpha shapes. "ACM Transactions on Graphics (TOG), 13(1):43–72.
- Evans, R., Marconi, U.M.B., Tarazona, P., 1986. Fluids in narrow pores: Adsorption, capillary condensation, and critical points. J. Chem. Phys. 84 (4), 2376–2399.
- Foresee, F. D. and Hagan, M. T. (1997). Gauss-newton approximation to bayesian learning. In Proceedings of international conference on neural networks (ICNN'97), volume 3, pages 1930–1935. IEEE.
- Fredlund, D.G., 2006. Unsaturated soil mechanics in engineering practice. J. Geotech. Geoenviron. Eng. 132 (3), 286–321.
- Fredlund, D.G., Morgenstern, N.R., 1977. Stress state variables for unsaturated soils. J. Geotech. Eng. Div. 103 (5), 447–466.
- Fredlund, D.G., Rahardjo, H., 1993. Soil mechanics for unsaturated soils. John Wiley & Sons.
- Fredlund, D.G., Xing, A., 1994. Equations for the soil-water characteristic curve. Can. Geotech. J. 31 (4), 521–532.
- Frenkel, D., Smit, B., 2001. Understanding molecular simulation: from algorithms to applications,, volume 1. Elsevier.
- Gens, A., 2010. Soil–environment interactions in geotechnical engineering. Geotechnique' 60 (1), 3–74.
- Goodfellow, I., Bengio, Y., Courville, A., 2016. Deep learning. MIT press.
- Hassanizadeh, S.M., Gray, W.G., 1990. Mechanics and thermodynamics of multiphase flow in porous media including interphase boundaries. Adv. Water Resour. 13 (4), 169–186.
- Houlsby, G., 1997. The work input to an unsaturated granular material. Geotechnique 47 (1), 193–196.
- Hoyos, L.R., Arduino, P., 2008. Implicit algorithm for modeling unsaturated soil response in three-invariant stress space. Int. J. Geomech. 8 (4), 266–273.
- Israelachvili, J.N., 2015. Intermolecular and surface forces. Academic press.
- Joekar-Niasar, V., Hassanizadeh, S., Leijnse, A., 2008. Insights into the relationships among capillary pressure, saturation, interfacial area and relative permeability using pore-network modeling. Transp. Porous Media 74 (2), 201–219.
- Jorgensen, W.L., Chandrasekhar, J., Madura, J.D., Impey, R.W., Klein, M.L., 1983. Comparison of simple potential functions for simulating liquid water. J. Chem. Phys. 79 (2), 926–935.
- Katti, D.R., Srinivasamurthy, L., Katti, K.S., 2015. Molecular modeling of initiation of interlayer swelling in na–montmorillonite expansive clay. Can. Geotech. J. 52 (9), 1385–1395.
- Leroy, F., Muller-Plathe, F., 2010. Solid-liquid surface free energy of lennard-jones liquid on smooth and rough surfaces computed by molecular dynamics using the phantom-wall method. J. Chem. Phys. 133 (4), 044110.
- Liang, J., Edelsbrunner, H., Fu, P., Sudhakar, P.V., Subramaniam, S., 1998. Analytical shape computation of macromolecules: I. molecular area and volume through alpha shape. Proteins Struct. Funct. Bioinf. 33 (1), 1–17.
- Likos, W.J., 2014. Effective stress in unsaturated soil: Accounting for surface tension and interfacial area. Vadose Zone J. 13 (5), 1–12.
- Likos, W.J., Song, X., Xiao, M., Cerato, A., Lu, N., 2019. Fundamental challenges in unsaturated soil mechanics. In: Geotechnical fundamentals for addressing new world challenges. Springer, pp. 209–236.

- Lourenc, o, S., Gallipoli, D., Augarde, C. E., Toll, D. G., Fisher, P. C., and Congreve, A. (2012). Formation and evolution of water menisci in unsaturated granular media. Geotechnique, 62(3):193–199.
- Lowry, M.I., Miller, C.T., 1995. Pore-scale modeling of nonwetting-phase residual in porous media. Water Resour. Res.  $31\ (3)$ , 455-473.
- Lu, N., 2016. Generalized soil water retention equation for adsorption and capillarity. J. Geotech. Geoenviron. Eng. 142 (10), 04016051.
- Lu, N., Likos, W.J., 2006. Suction stress characteristic curve for unsaturated soil. J. Geotech. Geoenviron. Eng. 132 (2), 131–142.
- Luo, S., Lu, N., Zhang, C., Likos, W., 2022. Soil water potential: A historical perspective and recent breakthroughs. Vadose Zone J. 21 (4), e20203.
- Macari, E.J., Hoyos, L.R., Arduino, P., 2003. Constitutive modeling of unsaturated soil behavior under axisymmetric stress states using a stress/suction-controlled cubical test cell. Int. J. Plast 19 (10), 1481–1515.
- MacKay, D.J., 1992. Bayesian interpolation. Neural Comput. 4 (3), 415-447.
- Menon, S., Song, X., 2020. Shear banding in unsaturated geomaterials through a strong nonlocal hydrome-chanical model. Eur. J. Environ. Civ. Eng. 1–15.
- Menon, S., Song, X., 2021. A computational periporomechanics model for localized failure in unsaturated porous media. Comput. Methods Appl. Mech. Eng. 384, 113932
- Menon, S., Song, X., 2022. Updated lagrangian unsaturated periporomechanics for extreme large deformatio in unsaturated porous media. Comput. Methods Appl. Mech. Eng. 400, 115511.
- Menon, S., Song, X., 2023. Computational coupled large-deformation periporomechanics for dynamic failure and fracturing in variably saturated porous media. Int. J. Numer. Meth. Eng. 124 (1), 80–118.
- Ng, C.W.W., Menzies, B., 2014. Advanced unsaturated soil mechanics and engineering. CRC Press.
- Nguyen, D., Widrow, B., 1990. In: Improving the learning speed of 2-layer neural networks by choosing initial values of the adaptive weights. IEEE, pp. 21–26.
- Nikooee, E., Habibagahi, G., Hassanizadeh, S.M., Ghahramani, A., 2013. Effective stress in unsaturated soils: A thermodynamic approach based on the interfacial energy and hydromechanical coupling. Transp. Porous Media 96 (2), 369–396.
- Niu, W.-J., Ye, W.-M., Song, X., 2020. Unsaturated permeability of gaomiaozi bentonite under partially free-swelling conditions. Acta Geotech. 15, 1095–1124.
- Peters, K.P., Fauck, J., Frommel, C., 1996. The automatic search for ligand binding sites in proteins of know three-dimensional structure using only geometric criteria. J. Mol. Biol. 256 (1), 201–213.
- Plimpton, S., 1995. Fast parallel algorithms for short-range molecular dynamics. J. Comput. Phys. 117 (1), 1–19.
- Ryckaert, J.-P., Ciccotti, G., Berendsen, H.J., 1977. Numerical integration of the cartesian equations of motion of a system with constraints: molecular dynamics of nalkanes. J. Comput. Phys. 23 (3), 327–341.
- Scocchi, G., Sergi, D., D'Angelo, C., Ortona, A., 2011. Wetting and contact-line effects for spherical and cylindrical droplets on graphene layers: A comparative moleculardynamics investigation. Phys. Rev. E 84 (6), 061602.
- Shi, B., Dhir, V.K., 2009. Molecular dynamics simulation of the contact angle of liquids on solid surfaces. J. Chem. Phys. 130 (3), 034705.
- Singh, R.K., Tropsha, A., Vaisman, I.I., 1996. Delaunay tessellation of proteins: four body nearest-neighbor propensities of amino acid residues. J. Comput. Biol. 3 (2), 213–221.
- Skipper, N.T., Chang, F.-R.-C., Sposito, G., 1995. Monte carlo simulation of interlayer molecular structurein swelling clay minerals. 1. methodology. Clay Clay Miner. 43 (3), 285–293.
- Song, X., 2017. Transient bifurcation condition of partially saturated porous media at finite strain. Int. J. Numer. Anal. Meth. Geomech. 41 (1), 135–156.
- Song, X., Wang, M.-C., and Zhang, K. (2018). Molecular dynamics modeling of unsaturated clay-water systems at elevated temperature. In The 7th International Conference on Unsaturated Soils 2018 (UNSAT2018)-Ng, Leung, Chiu & Zhou (Eds) The Hong Kong University of Science and Technology, ISBN 978-988-78037-3-7.
- Song, X., Wang, M.-C., 2019. Molecular dynamics modeling of a partially saturated claywater system at finite temperature. Int. J. Numer. Anal. Meth. Geomech. 43 (13), 2129–2146.
- Song, X., Ye, M., Wang, K., 2017. Strain localization in a solid-water-air system with random hetero-geneity via stabilized mixed finite elements. Int. J. Numer. Meth. Eng. 112 (13), 1926–1950.
- Song, X., Zhang, Z., 2021. Determination of clay-water contact angle via molecular dynamics and deep-learning enhanced methods. Acta Geotech. 1–15.
- Terzaghi, K., Peck, R.B., Mesri, G., 1996. Soil mechanics in engineering practice. John Wiley & Sons.
- Townsend, R.M., Rice, S.A., 1991. Molecular dynamics studies of the liquid-vapor interface of water. J. Chem. Phys. 94 (3), 2207–2218.
- Tuller, M., Or, D., Dudley, L.M., 1999. Adsorption and capillary condensation in porous media: Liquid retention and interfacial configurations in angular pores. Water Resour. Res. 35 (7), 1949–1964.
- Van Genuchten, M.T., 1980. A closed-form equation for predicting the hydraulic conductivity of unsaturated soils. Soil Sci. Soc. Am. J. 44 (5), 892–898.
- Vogl, T.P., Mangis, J., Rigler, A., Zink, W., Alkon, D., 1988. Accelerating the convergence of the back-propagation method. Biol. Cybern. 59 (4), 257–263.
- Wang, K., Song, X., 2020. Strain localization in non-isothermal unsaturated porous media considering material heterogeneity with stabilized mixed finite elements. Comput. Methods Appl. Mech. Eng. 359, 112770.
- Wheeler, S., Sharma, R., Buisson, M., 2003. Coupling of hydraulic hysteresis and stress-strain behaviour in unsaturated soils. Geotechnique 53 (1), 41–54.

Wildenschild, D., Vaz, C., Rivers, M., Rikard, D., Christensen, B., 2002. Using x-ray computed tomography in hydrology: systems, resolutions, and limitations. J. Hydrol. 267 (3–4), 285–297.

Wilson, J.A., Bender, A., Kaya, T., Clemons, P.A., 2009. Alpha shapes applied to molecular shape characterization exhibit novel properties compared to established shape descriptors. J. Chem. Inf. Model. 49 (10), 2231–2241.
Zhang, C., Lu, N., 2019. Unitary definition of matric suction. J. Geotech. Geoenviron. Eng. 145 (2), 02818004.